



**Nuno Filipe
Fernandes Caçoilo**

**Dinâmica de Comutação em Memórias Magnéticas
de Acesso Aleatório com Anisotropia de Forma
Perpendicular**

**Reversal Dynamics Driven by Spin Transfer Torque
in Perpendicular Shape Anisotropy Magnetic
Random Access Memories**



**Nuno Filipe
Fernandes Caçoilo**

**Dinâmica de Comutação em Memórias Magnéticas
de Acesso Aleatório com Anisotropia de Forma
Perpendicular**

**Reversal Dynamics Driven by Spin Transfer Torque
in Perpendicular Shape Anisotropy Magnetic
Random Access Memories**

Dissertação apresentada à Universidade de Aveiro para cumprimento dos requisitos necessários à obtenção do grau de Mestre em Engenharia Física, realizada sob a orientação científica do Professor Doutor Nikolai Andreevitch Sobolev, Professor Associado do Departamento de Física da Universidade de Aveiro, e sob a coorientação científica do Doutor Bernard Dieny, Investigador Principal do SPINTEC, CEA, Grenoble, França.

Apoio financeiro da Fundação para a Ciência e Tecnologia (FCT) através do projeto I3N/FSCOSD (Ref. FCT UID/CTM/50025/2019) e do *European Research Council (ERC)*, através da bolsa avançada *MAGICAL* número 669204

Cofinanciado por:



UNIÃO EUROPEIA
Fundo Europeu
de Desenvolvimento Regional



To the ones who supported me
and keep doing it

o júri / the jury

presidente / president

Prof.^a Doutora Margarida Maria Resende Vieira Facão

Professor Auxiliar do Departamento de Física da Universidade de Aveiro

arguente/appraiser

Prof. Doutor João Pedro Esteves de Araújo

Professor Auxiliar da Faculdade de Ciências da Universidade do Porto

orientador/supervisor

Prof. Doutor Nikolai Andreevitch Sobolev

Professor Associado do Departamento de Física da Universidade de Aveiro

agradecimentos

Agradeço ao Departamento de Física e ao I3N pelas oportunidades que me tem proporcionado ao longo da minha educação e, principalmente, durante esta tese de mestrado. Agradeço ao Professor Nikolai Sobolev pelo seu apoio, amizade e confiança em mim. Espero que a ligação que temos vindo a formar continue em trabalhos futuros. Agradeço ao Doutor Bernard Dieny, por me ter aceite e supervisionado no SPINTEC. Foi um orgulho trabalhar com um investigador tão reconhecido na área. Agradeço ainda ao futuro Doutor Bruno Teixeira, apesar de este ano não ter tido a sorte de ser meu coorientador, sempre me ajudou, mesmo à distância. Pela nanofabricação dos pilares de PSA-STT-MRAM agradeço ao Dr. Nicolas Perrisin, Dr. Steven Lequeux e Dr. Laurent Vila. Agradeço novamente ao Dr. Nicolas Perrisin e Mr. Gabin Grégoire pelos resultados de magnetoresistência. Agradeço à Dr. Liliana Buda Prejbeanu pela sua ajuda com as simulações micromagnéticas e ao Dr. Ricardo Sousa e Dr. Lucian Prejbeanu pelo apoio constante e supervisionamento.

Num tom informal, agradeço ao Alvaro, Daniel, Rafael, Steven e Marco, pela sua companhia nos nossos cafés de rotina. Agradeço ainda ao Pedro e ao Edmond, os meus companheiros na sala dos estagiários. Foi um prazer integrar-me com vocês no SPINTEC.

Por fim, agradeço aos meus pais, por permitirem que o filho esteja tanto tempo fora de casa e ao meu irmão Simão, por me fazer parar de estudar de vez em quando para ir brincar com ele. Agradeço ainda aos meus amigos, muitos para enunciar individualmente, mas vocês sabem quem são e, principalmente à Telma, pelo apoio constante, carinho, paciência e amizade.

Palavras Chave

Memória não volátil; STT-MRAM; anisotropia de forma perpendicular; asteróide com revolução 3D de Stoner-Wohlfarth; micromagnetismo; dinâmica de comutação da magnetização; movimento de parede de domínio transversal; tempo de comutação

Resumo

A memória magnética de acesso aleatório com uma anisotropia perpendicular é uma das mais promissoras memórias não voláteis (p-STT-MRAM). No entanto, estes dispositivos estão limitados pela sua estabilidade térmica a diâmetros superiores a 20 nm. Uma possível resposta a este problema baseia-se no uso da anisotropia de forma perpendicular, aumentando substancialmente a espessura da camada livre. Este método é aplicado num novo tipo de memórias, PSA-STT-MRAM. No entanto, como os pilares são fabricados com um *aspect ratio* elevado, alguns ficam inclinados durante o processo. De modo a interpretar corretamente as curvas de magnetoresistência, é importante saber com precisão a direção que o campo magnético aplicado faz com o eixo de simetria do pilar. Assim, um procedimento experimental baseado na análise de um asteróide de revolução 3D de Stoner-Wohlfarth é apresentado, permitindo o cálculo do ângulo de inclinação do pilar. A amostra estudada foi fabricada na *Plateforme de Technologie Amount* (PTA) em Grenoble, França, pelo grupo MRAM do SPINTEC. Simulações micromagnéticas foram realizadas para diferentes espessuras de camada livre, utilizando um código desenvolvido pela Liliana Buda Prejbeanu. A dependência do tempo e do modo de comutação com a voltagem aplicada é investigada. Foram observados dois regimes dinâmicos distintos para os parâmetros utilizados nas diferentes espessuras de camada livre de FeCoB. Para espessuras inferiores à de transição, verifica-se que a comutação exibe um modo de ondulação coletiva da magnetização. Para espessuras superiores verifica-se a nucleação e propagação de uma parede de domínio. Ambos estes regimes seguem uma relação linear entre a voltagem aplicada e o inverso do tempo de comutação, $V_{\text{aplicada}} \propto \tau_{\text{comutação}}^{-1}$. Simulações tendo em conta flutuações térmicas indicam que o modo de comutação é robusto com a introdução de temperatura no sistema. A compreensão do modo de comutação em memórias que usem o efeito de transferência de torque é importante para a fabricação de dispositivos otimizados, visto que a espessura da camada livre influencia tanto a estabilidade térmica como o tempo de escrita na memória.

Keywords

Non-Volatile Memory; STT-MRAM; Perpendicular Shape Anisotropy; 3D Stoner-Wohlfarth Astroid; Micromagnetism; Magnetization Reversal Dynamics; Transverse Domain Wall Motion; Switching time

Abstract

The perpendicular Spin Transfer Torque Magnetic Random Access Memory (p-STT-MRAM) is one of the most promising emerging non-volatile memory technologies. As these devices are limited by their thermal stability at technological nodes higher than 20 nm, their downsize capability is compromised. A possible answer to this problems relies on taking advantage of the shape anisotropy, by increasing substantially the thickness of the free layer. This method is employed in a new memory device, called Perpendicular Shape Anisotropy STT-MRAM (PSA-STT-MRAM). However, as pillar cells are nanofabricated with aspect ratios (AR) as high as 5, some elements become tilted during the process. In order to correctly interpret the magnetoresistance loops of individual elements, it is important to know the exact direction of the applied magnetic field with respect to the pillar symmetry axis. For this purpose, an experimental procedure based on a 3D Stoner-Wohlfarth astroid analysis is presented which allows to determine the tilt angle. The studied sample was fabricated in the *Plateforme de Technologie Amount* (PTA), in Grenoble, by the SPINTEC MRAM group. Additional micromagnetic simulations were carried out for different pillar thicknesses using a micromagnetic solver developed by Liliana Buda Prejbeanu, a researcher at SPINTEC. The behaviour of the switching time and reversal was analysed as a function of the applied voltage. Two distinct dynamical regimes were identified for simulation parameters for different FeCoB layer thicknesses. Below a thickness threshold, there is a collective curling-like reversal. Above it, the reversal happens through the nucleation and further propagation of a transverse domain wall. Both these regimes exhibit a linear dependence between the applied voltage and the inverse of the switching time, $V_{\text{bias}} \propto \tau_{\text{switch}}^{-1}$. Simulations performed including a stochastic thermal field indicate that the mechanism of reversal is robust against thermal fluctuations. In addition, it is observed that the magnetization reversal is controlled by STT and assisted by the thermal fluctuations. The understanding of the physical phenomena happening during the magnetization reversal driven by STT is important to engineer optimized devices, as the free layer thickness affects the thermal stability and the writing operation of the memory cell.

Contents

List of Figures	ii
1 Introduction	1
1.1 The need for emerging non-volatile memories	1
1.2 The road towards the Perpendicular STT-MRAM and beyond	3
1.3 Thesis Motivation	5
2 Theoretical concepts	7
2.1 Magnetic anisotropy	7
2.2 Magnetic domains	9
2.3 Spin transfer torque dynamics	10
3 Perpendicular shape anisotropy MRAM - a state of the art	14
4 From idea to conception of a PSA-STT-MRAM cell	16
4.1 Nanofabrication process	16
4.2 Determination of pillar tilt angle from 3D Stoner Wohlfarth astroïd analysis .	20
5 Micromagnetic analysis of the PSA-STT-MRAM	27
5.1 Micromagnetic model	27
5.2 Magnetization reversal in PSA-STT-MRAM	29
5.2.1 STT driven magnetization switching	30
5.2.2 Temperature study	42
6 Conclusions	46
References	48

List of Figures

1	Time-To-Market for STT-MRAM actors, by applications, for stand-alone and embedded memory types. The time scale represents the entrance into the STT-MRAM market. An effort done by different companies is expected for the embedded market, mostly on possibly replacing SRAM and the embedded Flash Technology. Figure extracted and modified from [14].	2
2	a) Sketch of a MTJ. The color of the layer depends on the orientation of the magnetization. Figure extracted from [20]. b) Necessary writing current to switch the magnetization in the free layer for the case of magnetic field writing (field MRAM) and STT writing (STT-MRAM), as a function of the cell size. Figure extracted from [21].	4
3	Thermal stability factor (Δ) as a function of the junction diameter for a p-STT-MRAM device. Adapted from [31].	6
4	(a) Magnetization dynamics of the LLG equation. (b) Switching trajectory for a p-STT-MRAM considering the spin-polarized current torque's contribution. Figure modified from [18].	10
5	Effect of the density of spin polarized current (\mathbf{J}) on two ferromagnetic layers of magnetization \mathbf{m}_{RL} and \mathbf{m}_{FL}	11
6	Stability diagram for a cylindrical storage layer, as a function of its total thickness (t) and Diameter (D). Values obtained at room temperature with literature values from [33]. The standard p-STT-MRAM encompasses $t < 3$ nm. Moreover, a thick black line is presented. The Δ values obtained after this line were done using micromagnetic simulations (MEP), as the switching mechanism is based on a domain wall nucleation and propagation. In the sketches, we see a usual p-STT-MRAM and the PSA-STT-MRAM, where the red thick storage layer is deposited. Figure adapted from [33]	15
7	Steps on the definition of the Ta Hard Mask (a - e) and of the MTJ pillar (g-h). Figures adapted from [58].	17
8	Schemes of the steps for defining the bottom (a-c) and top (d-g) electrodes and the electric contacts (h-j). Figure adapted from [58].	18
9	(a) Example of a final device, after the definition of the top and bottom electrodes. The pillar is unseen but it sits on the middle of the device. Scale of $2 \mu\text{m}$ (b) Full array of PSA-STT-MRAM, showing the density of the final device. Scale of $200 \mu\text{m}$. (c) Example of pillars before the electrodes are defined. We can observe straight, tilted and fallen pillars. Scale of 200 nm . SEM images obtained by the SPINTEC MRAM group at the PTA, Grenoble France. (d) Shadow effect originated from the etching step, promoting a decrease of the density of pillars in the device. Scale of 100 nm . Image extracted from [59].	19

10	Evolution of the resistance (R) as a function of \mathbf{H} for different field orientations (90° =field applied in the wafer plane, 0° =field applied normal to the wafer plane). The lines in red and black represent the cases where the field is applied orthogonal to the wafer plane (0° , i.e. along the expected easy axis if the pillar was perfectly perpendicular to the wafer) and parallel to the wafer plane (90° , i.e. along the expected hard plane if the pillar was perfectly perpendicular to the wafer), respectively. Inset: schematic representation of the experiment and frames from the laboratory (black) and wafer (blue). In this sketch, the PSA-STT pillar is assumed to be perfectly perpendicular to the wafer plane. Experimental results obtained by Nicolas Perrissin.	21
11	Schematic representation of the studied PSA-STT pillars. The thick Co (60 nm) layer is represented by the red color. (a) Representation of the pillar with its easy axis of magnetization aligned along the pillar axis. (b) Representation of a tilted pillar, the tilt is characterized by the tilt angle θ_{tilt} and azimuthal angle φ . The X and Y axes are in the plane of the wafer. (c) 3D Stoner Wohlfarth astroïd with revolution symmetry describing the switching field of the storage layer magnetization. The \mathbf{k}_{\parallel} direction corresponds to the easy-axis direction whereas $\mathbf{k}_{\perp 1}$ and $\mathbf{k}_{\perp 2}$ lie in the hard-plane.	22
12	Magnetoresistance loops as a function of \mathbf{H} for different orientation angles of the pillar axis. The insets represent sketch of the two experimental geometries. In the first configuration (a) the wafer rotation axis is the x-axis and the field is applied in the YZ plane. The maximum coercivity corresponding to \mathbf{H} within the hard plane is observed for an angle of $\theta_{\perp 1} = 95^\circ$. In the second configuration (b), the wafer rotation axis is the z-axis, and the field is applied in the XY plane. \mathbf{H} lies within the hard plane for $\theta_{\perp 2} = 40^\circ$. Experimental results obtained by Nicolas Perrissin.	23
13	Angular dependence of the two experimental situations of figure 12: (a) the wafer rotation axis is the x-axis and the field is applied in the YZ plane. (b) The wafer rotation axis is the z-axis and the field is applied in the XY plane. The blue squares represent the experimental results. The maximum coercivity H_{coercive} corresponding to a field applied in the hard-plane is marked with red stripes, the width of which corresponds to the experimental uncertainty. The green squares represent the coercivity values derived from a macrospin simulation of the hysteresis loops. Dashed black line: analytical variations derived from the 3D Stoner-Wohlfarth model.	24

14	a) Schematic representation of the studied FeCoB pillars with a thickness L and diameter of 20 nm. The effect of the iPMA is represented with blue arrows. The free layer is shown with a yellowish color, the tunnel barrier with a blue color and the reference layer with a reddish color. b) Equilibrium initial state of a thick layer of FeCoB (60 nm) without (left side) and with (right side) iPMA originated by the FeCoB/MgO interface. c) Representation of each elementary cell magnetization resorting to arrows. The color bar indicates the normalized magnitude of the magnetization along the defined \mathbf{z} direction (along the pillar axis) in each cell.	30
15	a) Dependency of the defined decay length (20 nm displayed with red spheres, 10 nm with blue spheres, 5 nm with yellow spheres and 2 nm with black spheres) for a normalized value of a_{\parallel} and K_u as a function of the pillar length. b) Polarization (P) and STT efficiency (η_{STT}) as a function of the TMR of the device.	31
16	a) Time dependency of $\langle m_z \rangle$ for a pillar thickness of 60 nm with square surface of 20 nm width. Results for different applied V_{Bias} (-1 V to -2 V) at $T = 0$ K. Frames of the magnetization dynamics during the reversal at V_{Bias} of a) -1 V and b) -1.1 V, at different time steps. Snapshots extracted using the Paraview Software.	33
17	Time representation of the dependency of $\langle m_z \rangle$ for different pillar thickness (30, 40, 50 and 60 nm) for different applied V_{Bias}	34
18	a) Values of STT switching current for different writing pulse widths. A ballistic and a thermal activation regime can be separated. Modified from [20]. b) Dependency of the applied V_{Bias} on (left panel) the switching time and (right panel) the inverse of the switching time. This shows a linear dependency $V_{\text{bias}} \propto \tau_{\text{switch}}^{-1}$. The different lengths are characterized with spheres of different colors. 30 nm is shown with a yellow color, 40 nm with a blue color, 50 nm with green and 60 nm with red.	35
19	a) Temporal dependency of the mean reduced magnetization $\langle m_z \rangle$ for different pillar thicknesses: 30 nm depicted with orange circles, 40 nm with blue squares, 50 nm with triangles and 60 nm with red circles. b) Temporal dependency of the different components of the magnetization. The mean reduced $\langle m_x \rangle$ is present with a black line, $\langle m_y \rangle$ with a red line and $\langle m_z \rangle$ with a blue line. Results obtained for a V_{Bias} of -2.5 V.	36
20	Switching trajectory for a thick layer of 30 nm (red points), 40 nm (blue points), 50 nm (golden points) and 60 nm (green points). The z axis represents $\langle m_z \rangle$ and the basal plane (x and y axis) represents $\langle m_{x,y} \rangle$. The simulated data is contained in a macrospin sphere (radius 1). Results obtained for V_{bias} of -2.5 V.	37

21	<p>Snapshots at different time steps for a 30, 40, 50 and 60 nm thick magnetic layer, for an applied voltage of -2.5 V. The $\tau_{\text{nucleation}}$, $\tau_{50\%}$ and $\tau_{90\%}$ are shown at bold. The color is representative of the magnitude of \mathbf{m}_z and quantified in the color plot. It is observed a collective curling-like reversal for thicknesses of 30 and 40 nm. For 50 and 60 nm the reversal mechanism is based on a transverse domain wall nucleation and propagation.</p>	38
22	<p>Evolution of the Domain Wall Motion behaviour for thickness of 40 nm to 60 nm with an applied voltage of -2.5 V. The mean reduced magnetization $\langle m_z \rangle$ is displayed for each pillar thickness.</p>	39
23	<p>Dependence of the a) mean reduced energies of the magnetic system, normalized by the maximum value of the total energy (E_{total} shown with blue spheres, E_{exchange} with red circles, E_{Ku} with blue triangles and E_{shape} with orange squares) and b) the process time ($\tau_{\text{nucleation}}$ shown with orange squares, $\tau_{50\%}$ with blue triangles and, with red circles, $\tau_{90\%}$ as a function of the pillar thickness for an applied voltage of -2.5 V.</p>	40
24	<p>a) Effect of the mesh grid on the reversal mechanism of a squared (2 nm mesh with a blue color and 1 nm mesh with light blue) and circular (2 nm mesh with a red color and 1 nm with orange color) shaped pillar. For all cases the used value of a_{\parallel} is of 0.08 T/V. b) Shape of the pillar surface for 2 nm mesh and 1 nm mesh circular based pillar.</p>	41
25	<p>Time evolution of a) 100 events of the mean reduced magnetization $\langle m_z \rangle$ at different applied voltages (from left to right, -2 V, -3 V and -4 V) b) The distribution of the different process, associated with each magnetization curves. The histograms are realised with 0.25 bin size and are enveloped with a log-normal distribution curve. $\tau_{\text{nucleation}}$ is shown with a red colour, $\tau_{50\%}$ with a blue curve and $\tau_{90\%}$ with orange color. Results obtained for a temperature of 300 K and pillar thickness of 60 nm and 20 nm diameter.</p>	43
26	<p>Applied voltage as a function of the process time ($\tau_{\text{nucleation}}$, $\tau_{50\%}$ and $\tau_{90\%}$) and of the inverse of the process time. $\tau_{\text{nucleation}}$ is depicted with a red color, $\tau_{50\%}$ with blue color and and $\tau_{90\%}$ with orange color. Results obtained for a pillar thickness of 60 nm and diameter of 20 nm for a temperature of 300K.</p>	43
27	<p>Lognormal distribution for the different processes. With a red color the $\tau_{\text{nucleation}}$ is identified, with blue the $\tau_{50\%}$ and, with orange, $\tau_{90\%}$. Evolution for temperatures ranging 100 K until 350 K (50 K step). Results obtained for a 60 nm thick pillar with diameter of 20 nm for an applied bias of -2.5 V. Bin size of 0.25 ns.</p>	44
28	<p>Different process time (ns) for a Temperature evolution (from 0 K to 350 K). With red circles we observe $\tau_{\text{nucleation}}$, blue squares the $\tau_{50\%}$ and orange triangles $\tau_{90\%}$. The data points are fit with an exponential function.</p>	45

29 Applied voltage as a function of the process time (ns) and the inverse of the process time. The $\tau_{\text{nucleation}}$ is depicted with a red color, the $\tau_{50\%}$ with blue color and $\tau_{90\%}$ with orange color. Results obtained for a thickness of 30 nm with a diameter of 20 nm for a temperature of 300K. 45

1 Introduction

1.1 The need for emerging non-volatile memories

The demand for an improvement in data handling has been growing exponentially during the last decades. Following the onset of high-performance computing and social networking, the memory market is tackling the needs for higher storage capacity, data treatment speed and energy consumption. Moreover, the constant miniaturization of the devices is pursued, and it is the latest complication regarding the Moore's law. Able to predict that the number of transistors would double about every 2 years, Moore's law now faces a downsize scalability limit. The microelectronics industry has been focusing efforts to tackle these current challenges for memory improvement, and a possible answer resides in the development of emerging non volatile memories (e-NVM) [1,2]

In this chapter, a brief introduction into the evolution of the memory technology is presented, focusing on the successive improvements of writing speed and endurance. The challenges facing the ubiquitous memories of nowadays, that ultimately lead to the emergence of new memories, will be explained with particular focus on the Magnetic Random Access Memory (MRAM), on the corresponding methods of writing information, from applied magnetic field to the use of the spin-transfer-torque effect and to the novel concept of Perpendicular Shape Anisotropy Spin Transfer Torque Magnetic Random Access Memory (PSA-STT-MRAM), which is the focus of this thesis.

Memory devices are normally divided in two major groups, regarding their applications. The first one is the stand-alone memory, which acts as an external component to the main unit and offers a high storage capacity. Its operation ranges from industry (*e.g.* automotive, sensor applications) to mass storage (*e.g.* USB sticks and Solid State Drives (SSD)). The second group is the embedded memory which is a part of the main unit. Its storage capacity is smaller than that of the stand-alone and it finds application in mobile devices, cache and Micro-Controller units devices (*e.g.* smart cards). Within those fundamental groups we can find different memory types. The stand-alone group is dominated by the FLASH (NAND) technology and the embedded memory group by the Static RAM (SRAM) and Dynamic RAM (DRAM). The first one is termed as a non-volatile memory, as it retains information even when powered off, while the last two are labelled as volatile memories, as they lose information when turned off. In order to explain the differences in the intrinsic properties of these distinct devices, a hierarchic system can be adopted. From this point we can divide the top- (SRAM and DRAM) and bottom-tier (Flash, HDD, SDD) of the pyramid as **hot-storage** and **cold-storage**, respectively, depending on how often they are accessed. The **hot-storage** presents a very high writing speed, low size (required since they are classified as embedded memories) and they are quite expensive. In contrast, the **cold-storage** does not possess a high writing speed but, being an external component, presents a larger storage capability and a lower cost [3,4].

One vital parameter when describing a memory is its endurance, which reflects the number of times the memory can be used before becoming defective. The top-tier memories offer

higher endurance than the bottom-tier ones [5,6]. Upon analysis of these different parameters, a gap between the top- and bottom-tier is found, which can be filled by the storage class memory (SCM). This gap opens the possibility of memories with writing speed and endurance near the ones of DRAM and SRAM alongside the low cost and high density of the FLASH [4].

With the constant growth of data, the SCM market finds itself as the most suitable application-price range memory, estimating a revenue doubling every year [3]. Thus, the research of new memory types, adapted to this storage class, is of utmost importance. A possible answer to this memory demand are the novel e-NVM. In addition to being non-volatile (*i.e.* not requiring power to retain information), they offer a higher density and endurance than the FLASH. Adding to this, the e-NVM memories offer a scalability advantage [7].

As previously stated, the memory class can be first divided as volatile and non-volatile. The volatile class comprises the usual DRAM and SRAM. The non-volatile class encompasses e-NVM and some standard memories, such as the FLASH and NVSRAM (non-volatile SRAM [8]). Inside the e-NVM the most promising technologies are the Ferroelectric RAM (FeRAM) [9, 10], Resistive RAM (RRAM) [11, 12], Phase-Change RAM (PCRAM) [13] and the Spin Transfer Torque Magnetic RAM (STT-MRAM). Even though none of these e-NVM shows

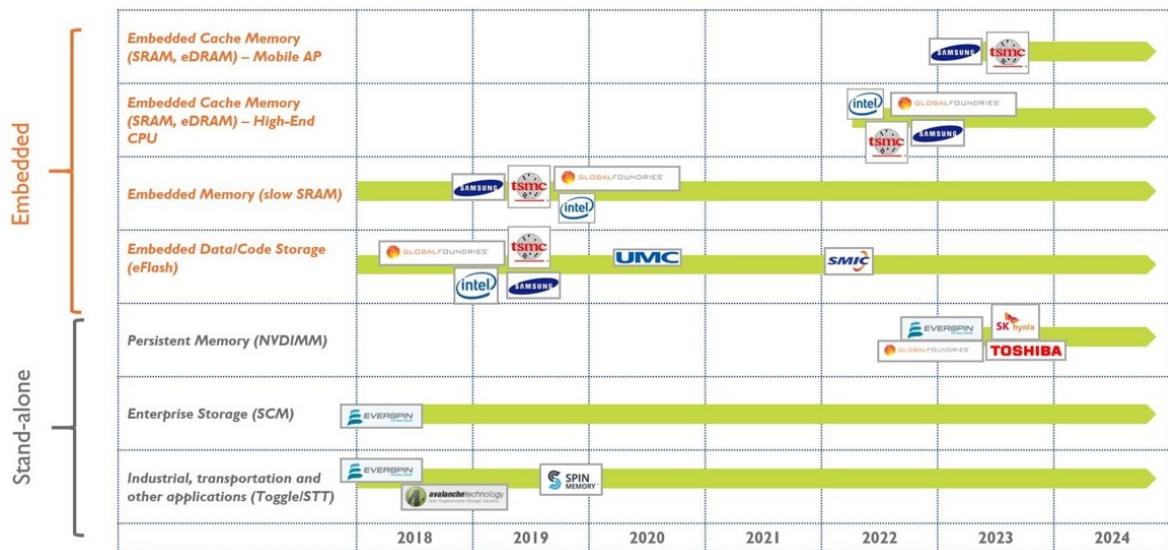


Figure 1: Time-To-Market for STT-MRAM actors, by applications, for stand-alone and embedded memory types. The time scale represents the entrance into the STT-MRAM market. An effort done by different companies is expected for the embedded market, mostly on possibly replacing SRAM and the embedded Flash Technology. Figure extracted and modified from [14].

an optimal set of parameters (such as endurance, size and writing speed), depending on each application, they could replace standard memories. For instance, the DRAM could be replaced by the STT-MRAM. Their speed is comparable, and the STT-MRAM is non-volatile, bringing more advantages. However, its price is substantially higher, being a substantial disadvantage. Compared with the FLASH memory, all the shown e-NVM show a good set

of parameters. Nevertheless, the FLASH technology is quite inexpensive, being difficult to replace [15].

Nowadays we are witnessing an expansion of the MRAM memory market. Forbes [16] predicts that the market of the e-NVM will reach \$20 Billion by 2029. One important point to be noticed is the drastic increase (compared with the other e-NVM types) in the MRAM revenues (expected to be dominated by the STT-MRAM) by 2029, with estimated revenues reaching around \$4 billion, a $170\times$ increase compared to 2018 [4, 16]. This prediction can be seen as a growth in the maturity of the technology and explains the companies entering in this highly competitive field. A diagram with the time-to-market perspective for each of these companies can be seen in figure 1.

Even though the market viewpoint shows a promising future for this memory, a constant study and improvement of this technology is of the most importance. Thus, it is important to revisit the first MRAM families and observe how they evolved and what can we expect from future engineering structures. For this purpose, an historical perspective of the road of the MRAM technology is shown and, lastly, the state of the art of the technology, exhibiting a competitive prospect for this research field.

1.2 The road towards the Perpendicular STT-MRAM and beyond

The MRAM consists on the magnetic tunnel junction (MTJ), one of the most prevalent device in the field of spintronics, whose main characteristic is the combined manipulation of the spin and charge of the electrons [17]. This memory device enables the discrimination of the bits **1** and **0** through the relative orientation of the magnetization in ferromagnetic layers, separated by an insulator layer, usually crystalline MgO. One of the magnetic layers has its magnetization pinned, behaving as a reference layer (RL). The other allows the manipulation of its magnetization, making possible the storage of information, being then denominated storage layer or free layer (FL). The insulator layer is called tunnel barrier (TB). When thin enough (typically less than 2 nm [18]), it enables the tunnelling of electrons. The resistance of the device is associated with the relative orientation of the magnetization in the two ferromagnetic layers. The higher the difference in resistance, the easier it is to read the information in the device. This difference in resistance states defines the tunnel magnetoresistance (TMR)

$$\text{TMR} = \frac{R_{\text{AP}} - R_{\text{P}}}{R_{\text{P}}}, \quad (1)$$

where R_{AP} is the resistance associated with the anti-parallel state of magnetizations and R_{P} the resistance state associated with the parallel state. Enhancing the crystallization of the layers promotes the tunnelling of spin polarized electrons, increasing the polarization efficiency. Thus promoting an increase on TMR, with values as high as 600% being reported [19]. This phenomena can be understood through analysis of figure 2 a). Two ferromagnetic layers are displayed (in red and blue regarding their spin orientation), separated by a tunnel barrier. Due to quantum tunnelling a spin-polarized current will flow from the RL to the FL, as depicted by the direction of the density of current (\mathbf{J}). When both magnetizations are

parallel, there is a good band matching, allowing transport from majority bands to majority bands and from minority bands to minority bands. This results in a high current, linked with a low resistance. In contrast, for an anti-parallel magnetization state, the transport occurs from a majority band to a minority band and vice-versa, resulting in a low current passing through, associated with a high-resistance state.

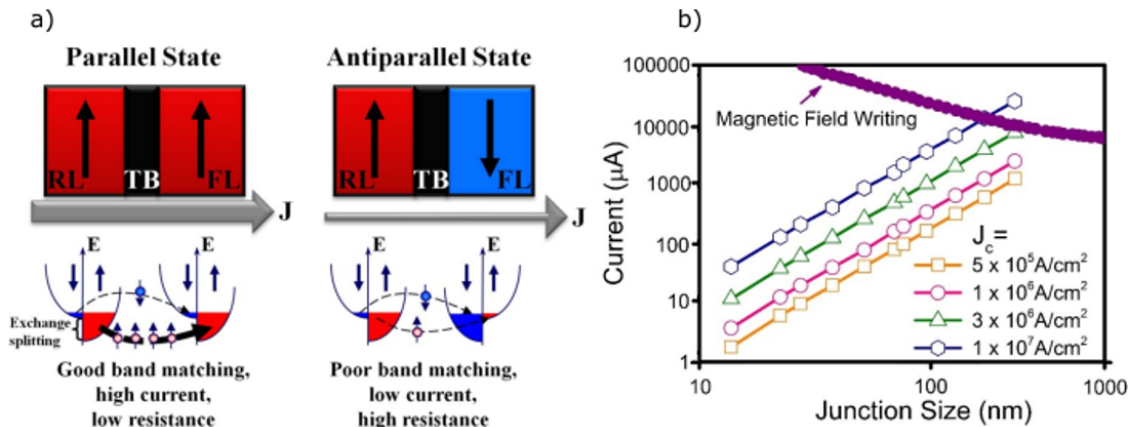


Figure 2: a) Sketch of a MTJ. The color of the layer depends on the orientation of the magnetization. Figure extracted from [20]. b) Necessary writing current to switch the magnetization in the free layer for the case of magnetic field writing (field MRAM) and STT writing (STT-MRAM), as a function of the cell size. Figure extracted from [21].

For our MTJ to be a working memory device there are several key requirements it must satisfy. Obviously, we must be able to write data on the memory, store it and then read it when necessary. Even though the working principle is conceptually the same, there are different families of MRAM, which have been improving in the last years. In these different families the reading method is quite similar among them, carried out by measuring the difference in resistance between two different states of the device (usually, for a working device, it is necessary a cell with $\text{TMR} > 200\%$ [20]). The information storage is dependant on the intrinsic magnetic properties of the storage layer, and is characterized by the thermal stability factor Δ , which defines how long the memory chip can retain the information (retention time). This factor is crucial for a working device and should be $\Delta > 60$ (for a 10 year retention in a 1Gbit memory chip at room temperature), determined by the energy barrier (E_B) that must be overcome for the magnetization in the FL to switch to the opposite direction (while turned off), divided by the thermal activation energy, defined as the product between the Boltzmann constant, k_B , (of value $1.38 \times 10^{-23} \text{ m}^2 \text{ kg s}^{-2} \text{ K}^{-1}$) and the working temperature, T [18,22]

$$\Delta = \frac{E_B}{k_B T}. \quad (2)$$

The main distinction between the different MRAM families is the way in which the information is written, being one of the most researched aspects in this technology. In a first generation, the writing process required an external applied magnetic field to rotate the

magnetization orientation in the FL. However, as the size of the memory cell decreases, a higher field is required to do the switching, resulting in a higher current through the selection lines and consequent increased power consumption [18]. An alternative method consists in the use of a spin-polarized current, relying on the spin-transfer-torque (STT) effect. MRAMs based on this effect are called STT-MRAM and achieve a lower power consumption at increased bit densities as the current for the writing scales down with the device dimensions [23]. This contrast can be seen in figure 2 b). As the focus turns to STT based devices, different branches arise. In a first approach, the magnetization was oriented in the plane of the film. However, it has been shown that a perpendicular orientation of the magnetization leads to an increase in thermal stability and reduction of the switching current. These devices are called perpendicular STT-MRAM (p-STT-MRAM) and use the interfacial perpendicular magnetic anisotropy (iPMA) originated from the interface between FeCoB layer and the MgO tunnel barrier [24]. Additional improvements in switching speed and power consumption are expected to be attained by misaligning the magnetization by a certain angle away from the perpendicular direction, making use of a canting configuration, known as easy-cone state. Such an easy-cone was observed in FL of MgO/FeCoB/Ta [24–29] but only for a certain range of thicknesses, located in the crossover from the in-plane (IP) to the out-of-plane (OOP) anisotropy.

Even though they are still in an early phase of its development, other memory architectures are being developed (Voltage Controlled MRAM and Spin Orbit Torque MRAM), showing quite promising results, and posing as possible candidates for improved spintronic-memory devices [18, 20, 21].

1.3 Thesis Motivation

As far as commercial capability goes, STT-based switching in p-MTJ is the most promising for MRAM technology. Nonetheless, this technology is not without flaws. There are still some major challenges, predominately when the MTJ dimension goes to sub-20 nm diameter. As the device shrinks, there is a decrease in the thermal stability due to a decrease in the free layer volume, as seen in figure 3. This decrease reduces significantly the retention time of the memory [30–32]. Since these devices are limited by their thermal stability at low dimensions, the downsize capability of the p-STT-MRAM is compromised. This limitation can be understood considering the different anisotropy sources in the storage layer. As the magnetostatic anisotropy tends to align the magnetization in an in-plane direction, the iPMA should counter, and overcome, this effect, bringing the magnetization in an OOP orientation. However, when the diameter of the cell is reduced, the total magnitude of the iPMA will be, in consequence, reduced as well. Therefore, this constant competition between the IP and OOP magnetization orientations is limiting the free-layer diameter. Thus, shrinking the device will lead to a decrease of the thermal stability. A promising answer to this problem is a novel structure that takes advantage of the shape anisotropy of the storage layer by increasing its thickness. Employing this idea, the shape anisotropy will no longer try to align

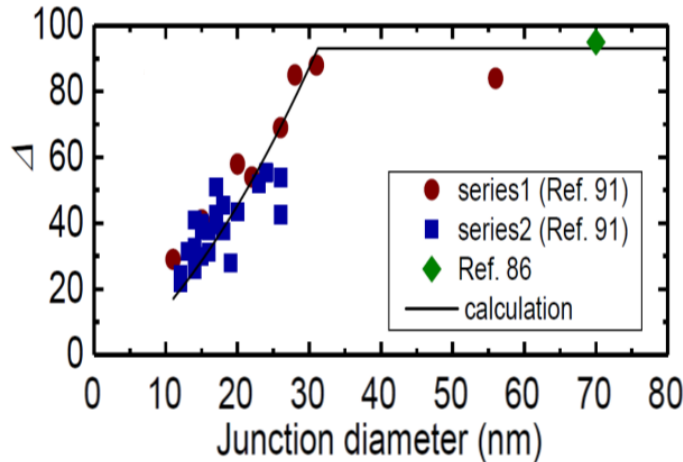


Figure 3: Thermal stability factor (Δ) as a function of the junction diameter for a p-STT-MRAM device. Adapted from [31].

the magnetization in an in-plane direction, supporting the perpendicular induced anisotropy in bringing the magnetization in a perpendicular configuration. This memory cell adopts the name Perpendicular Shape Anisotropy STT-MRAM, and studies made on working devices were already published by SPINTEC [33] and Tohoku University [34].

In this dissertation, a study on this novel and promising branch of STT-based MRAM is implemented in collaboration with SPINTEC, Grenoble. Furthermore, we divide this work in two distinct sections. The first part regards processes related with the nanofabrication and stack engineering of these memory cells, being a more experimental chapter. Here, an experimental procedure based on a 3D Stoner-Wohlfarth asteroïd analysis is implemented to measure the tilting angle of possible tilted pillars, which might happen considering their high aspect ratio (AR). This work was made as an extension of the experimental results already obtained by Nicolas Perrissin and Gabin Grógoire, resulting in a publication in the Journal of Applied Physics [35].

As the thickness of the storage layer grows larger, the magnetization is expected to be more stable due to the sturdy effect of the shape anisotropy. This is obtained due to the associated high values of thermal stability [33,34]. Furthermore, as these values grow larger, the current necessary to switch the free-layer magnetization resorting to a spin polarized current increases, consequently. Therefore, for further material and stack development, it is important to understand the reversal mechanism in this type of devices. For this purpose, in the second part of this work, micromagnetic simulations are carried out for different pillar thicknesses, using a micromagnetic solver developed by Liliana Buda Prejbeanu, a researcher at SPINTEC. The dependence of the switching time and reversal behaviour is analysed as a function of the applied voltage, with and without the effect of thermal fluctuations.

2 Theoretical concepts

To fully understand and explain this novel concept of PSA-STT-MRAM, a first explanation of some basic notions of magnetic anisotropy and spin-transfer-torque dynamics is required.

2.1 Magnetic anisotropy

There are cases where, when describing magnetic properties of matter, no considerations are made regarding the relative orientation of the external applied field and particular orientations of the magnetized body. This case happens when the system is considered isotropic, *i.e.* measurements of magnetic characteristics would yield the same value regardless of the chosen direction. However, in most real cases this is not true, and the material is said to possess magnetic anisotropy, being more easily magnetized to saturation when the magnetic field is applied along one direction (easy axis) than other directions (hard axis). The anisotropy energy ($E_{\text{anisotropy}}$) can be imagined as an energy barrier which must be overcome to rotate the magnetization from the easy-axis to a hard-axis.

Overlooking their origin, the different uniaxial anisotropy contributions can be described by an energy per unit of volume

$$E_{\text{anisotropy}} = -K_u(\hat{\mathbf{n}} \cdot \mathbf{m})^2, \quad (3)$$

where K_u is an uniaxial anisotropy energy constant, $\hat{\mathbf{n}}$ is the unitary vector of the easy axis direction and \mathbf{m} a unitary vector defining the magnetization, \mathbf{M} , direction [20].

Even though there are different anisotropy sources, a focus is made on the shape anisotropy (necessary to introduce the concept of PSA-STT-MRAM and present in all MRAM devices), bulk anisotropy (for example, magnetocrystalline anisotropy) and interface-related anisotropy.

Shape anisotropy

The shape anisotropy is a type of magnetic dipolar anisotropy known for its long-range interaction [36]. It is known that a magnetized body produces an intrinsic magnetic field. This can be interpreted as if magnetic charges were left at the surface of the ferromagnetic material (conceptual convenience), similar to the case of an accumulation of electric charges on the surface of the electrode of a capacitor, producing a magnetic field pointing in a direction opposite to that of the magnetization, known as the demagnetizing field $\mathbf{H}_{\text{demag}}$ [37]. This field is related with \mathbf{M} through

$$\mathbf{H}_{\text{demag}} = -\mathcal{N} \cdot \mathbf{M}, \quad (4)$$

where \mathcal{N} is a diagonal tensor, with a trace of 1.

The calculation of this field can be extremely difficult for a ferromagnet of arbitrary shape,

but it is straightforward for an uniformly magnetized ellipsoidal ferromagnet. When \mathbf{M} is parallel to one of the axis of the ellipsoid, \mathcal{N} is a number, characterized as the demagnetizing factor. Taking into consideration the demagnetizing field, we then obtain

$$E_{\text{shape}} = -\frac{1}{2}\mu_0 \int_V \mathbf{M} \cdot \mathbf{H}_{\text{demag}} \, dV. \quad (5)$$

where μ_0 is the vacuum permeability ($4\pi \times 10^{-7}$ H/m).

After some manipulation (resorting to properties from the Maxwell equations and the density of magnetic energy) we rewrite the energy of the shape anisotropy as

$$E_{\text{shape}} = \frac{1}{2}\mu_0\mathcal{N}(\hat{\mathbf{n}} \cdot \mathbf{M})^2 \quad (6)$$

Other anisotropy sources

Moving forward, we can discriminate the bulk and interfacial anisotropy energy contributions as, respectively,

$$E^{\text{bulk}} = -K_V(\hat{\mathbf{n}} \cdot \mathbf{M})^2, \quad (7)$$

and

$$E^{\text{interface}} = -\frac{K_s}{L}(\hat{\mathbf{n}} \cdot \mathbf{M})^2, \quad (8)$$

where K_V is a volume energy (J/m³), K_s a surface anisotropy (J/m²) and L the thickness of the magnetic layer [20].

One of the examples of the bulk anisotropy is the magnetocrystalline anisotropy (MCA), mainly arising from the spin-orbit coupling [36]. When this anisotropy is not purely uniaxial, additional terms must be considered. For instance, in an hexagonal structure, such as the case of Co, the MCA term can be written as

$$E_{\text{MCA}} = k_1 \sin^2 \theta + k_2 \sin^4 \theta, \quad (9)$$

where we define k_1 and k_2 as the first- and second-order anisotropy energy constants and θ the angle between the magnetization vector and the principal axis of symmetry. If we were to consider some anisotropy related with the basal plane, this description would require sixth order terms [36,38]. Therefore, the symmetry of the MCA is closely linked to the symmetry of the crystalline structure.

The last relevant magnetic anisotropy is the one of interfacial origin. This effect can occur at the interface of two different materials, where one of them is a ferromagnet. For certain combinations this anisotropy favours the alignment of the magnetization in a direction perpendicular to the plane. This possibility opened the doors to the p-STT-MRAM, being therefore heavily researched [20,29,36]. Combinations of Co/Pt and Co/Pd are known for having strong perpendicular magnetic anisotropy (PMA), related to an increase in the orbital momentum of the magnetic transition metal due to the strong hybridization between the 3d orbitals (of the transition metal) and the 5d orbitals (of the non-magnetic transition metal).

This hybridization induces a charge transfer between the two layers which, combined with a strong spin-orbit coupling, leads to a PMA. Moreover, the MRAM structure design was heavily impacted with the discovery of the iPMA arising from the overlap of the 3d orbitals of Fe and the 2p orbitals of O at the FeCoB/MgO interface [43, 44].

It is quite straightforward that, by varying the different anisotropy sources, the magnetization in the material will align in the plane of the film or perpendicular to it, respectively, an IP-STT-MRAM and p-STT-MRAM.

2.2 Magnetic domains

When the magnetization is aligned according to some easy axis, as a result of the competition from the different anisotropies, it will create a stray field outside of the main ferromagnetic body. The magnetic material will try to reach the minimum energy state by reducing this outside stray field, as it makes some contribution to the magnetostatic energy. One way to do so is to break the material into magnetic domains, as proposed by Weiss [45]. For instance, if the material breaks into two domains the magnetostatic energy will be reduced because it will bring the magnetic poles closer to each other [46]. However, as we are considering that the magnetic domains appear inside the material as a result of short-range interaction, we must also account for the exchange energy which does not favour the appearance of domains at all, as it is minimized when neighbouring magnetic moments are parallel. This energy term is then written as

$$E_{\text{exchange}} = -\mathcal{J} \sum_{i,j} \mathbf{S}_i \cdot \mathbf{S}_j, \quad (10)$$

where \mathcal{J} is the exchange integral (positive for a ferromagnetic coupling) and $\mathbf{S}_{i,j}$ the spin of neighbouring magnetic moments. This means that the appearance of a magnetic domain wall, the region inside a magnetic body between domains with different orientations, comes with an energetic cost, with the final result originating from the competition between magnetostatic and exchange energy. Considering different magnetic moments separated at the point where they do not interact with each other, the magnetostatic energy will overrule the exchange energy. Thus, in order to decrease the magnetostatic energy, small and incremental angular reorientations of the neighbouring spins between the two non-interact magnetic moments, could decrease the magnetostatic energy, without increasing too much the exchange energy. These reorientations occur within the magnetic domain wall. Lastly we contemplate the MCA of the material. Considering that the magnetization is initially aligned with an easy axis, the MCA will try to enforce a thin wall (Néel wall), where the vector change is abrupt, resulting in a reduced MCA but high exchange energy. Sometimes the exchange energy is low and the MCA is high, resulting in a thick wall (Bloch wall). Thus the sizes and patterns of domains and domain walls, such as for example, a wall closure, are determined by an equilibrium state defined by a fine balance between different anisotropies, such as magnetocrystalline, magnetostatic and exchange [37, 45, 46].

2.3 Spin transfer torque dynamics

The idea of the reversal of the magnetization of a magnetic layer using a spin-polarized current due to the STT effect was first predicted by Slonczewski [47] and Berger [48] in 1996. In 2004 this effect was first measured in a MTJ [49]. This idea of a spin polarized current interacting with the magnetization of the free layer can be translated as an equation of motion, as additional terms to the conventional magnetization dynamics.

As the free layer is a ferromagnetic material, we must take into account the effective magnetic field \mathbf{H}_{eff} , which includes a possible applied magnetic field \mathbf{H}_{app} , anisotropy fields \mathbf{H}_K , the demagnetization field $\mathbf{H}_{\text{demag}}$ and existent stray fields arising from adjacent magnetic layers. As a first approach, we consider that all the magnetic moments inside the body rotate coherently towards a sufficiently strong external magnetic field. This approximation receives the name macrospin, as the ferromagnetic body has as an uniform magnetization described by a direction and a magnitude (its saturation magnetization M_s). This model can be used in cases where the volume of the ferromagnetic material decreases down to the point where the formation of domain walls is energetically not favoured. In addition, the exchange energy term, equation (10) can be considered as a constant value in the total energy of the system, as long as the macrospin approximation remains valid.

The motion of a macrospin with respect to \mathbf{H}_{eff} is conceptualized in the known Landau-Lifshitz-Gilbert (LLG) equation

$$\frac{d\mathbf{m}}{dt} = \underbrace{[-\gamma\mu_0\mathbf{m} \times \mathbf{H}_{\text{eff}}]}_{\Gamma_{\text{precession}}} + \underbrace{[-\alpha\gamma\mu_0\mathbf{m} \times (\mathbf{m} \times \mathbf{H}_{\text{eff}})]}_{\Gamma_{\text{damping}}} \quad (11)$$

where \mathbf{m} is the normalized magnetization vector, \mathbf{H}_{eff} the effective magnetic field, α is the total damping experienced by the magnetization, γ the gyromagnetic ratio and μ_0 the vacuum permeability [18, 50]. From the LLG dynamics, equation (11), we can realise that the first

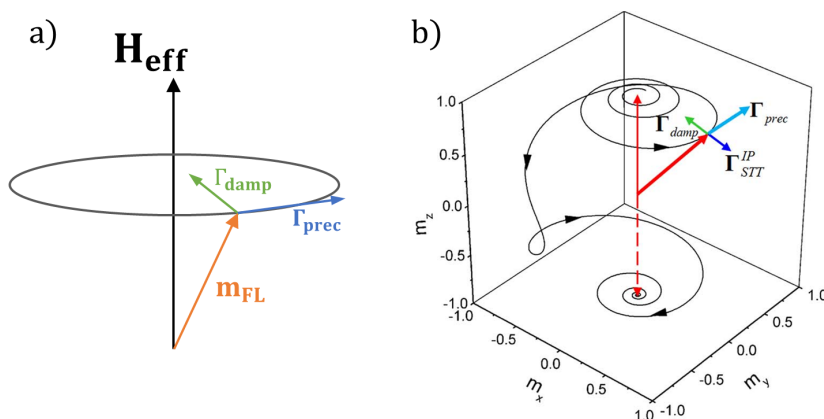


Figure 4: (a) Magnetization dynamics of the LLG equation. (b) Switching trajectory for a p-STT-MRAM considering the spin-polarized current torque's contribution. Figure modified from [18].

term, $\Gamma_{\text{precession}}$, acts as an undamped precession of \mathbf{m} around \mathbf{H}_{eff} , with a frequency equal

to the Larmor frequency, $\omega_{\text{Larmor}} = g \frac{2e}{2m_e} B$, where g is the g -factor of the electron, e is the electron charge and m_e its mass [37]. The second term, Γ_{damping} , represents a damping of this precession (defined by α), that will reduce $\mathbf{m} \times \mathbf{H}_{\text{eff}}$ until \mathbf{m} aligns with \mathbf{H}_{eff} . This effect can be seen in figure 4 a) for the case of the magnetization in the free layer.

In a STT-MRAM the switching is achieved through a spin-polarized current [47,48]. When a non-polarized current crosses the reference layer, it gains the direction of the magnetization in that layer. The polarized electrons are now transmitted throughout the tunnel barrier and exert a torque on the magnetization of the free layer. This phenomena is visualized in the diagram of figure 5. The STT phenomenon is introduced in the typical LLG equation as two

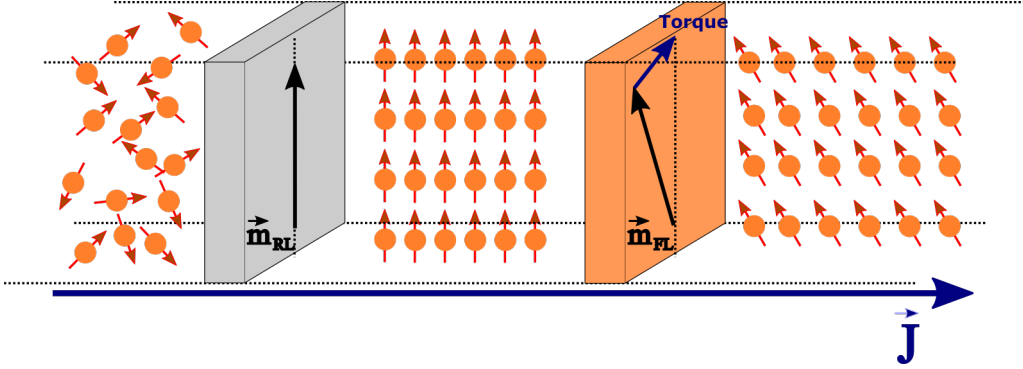


Figure 5: Effect of the density of spin polarized current (\mathbf{J}) on two ferromagnetic layers of magnetization \mathbf{m}_{RL} and \mathbf{m}_{FL} .

additional torque terms, the IP torque (or damping-like torque), $\Gamma_{\text{STT}}^{\text{IP}}$, and the OOP torque (or field-like torque), $\Gamma_{\text{STT}}^{\text{OOP}}$. The resulting equation with added STT is called LLGS (LLG Slonczewski) equation of motion and has the following representation

$$\frac{d\mathbf{m}_{\text{FL}}}{dt} = \Gamma_{\text{precession}} + \Gamma_{\text{damping}} + \Gamma_{\text{STT}}$$

with

$$\Gamma_{\text{STT}} = \underbrace{\left[-\gamma\mu_0\eta_{\text{STT}} \frac{\hbar J}{2e} \frac{1}{M_s L} \mathbf{m}_{\text{FL}} \times (\mathbf{m}_{\text{FL}} \times \mathbf{m}_{\text{RL}}) \right]}_{\Gamma_{\text{STT}}^{\text{IP}}} + \underbrace{\left[\gamma\mu_0\eta'_{\text{STT}} \frac{\hbar J}{2e} \frac{1}{M_s L} \mathbf{m}_{\text{FL}} \times \mathbf{m}_{\text{RL}} \right]}_{\Gamma_{\text{STT}}^{\text{OOP}}}, \quad (12)$$

where J is the current density, L the FL thickness, e the electron charge, η_{STT} the STT efficiency (\propto TMR), \hbar the reduced Planck constant and \mathbf{m}_{RL} the normalized vector defining the pinned magnetization in the reference layer.

It is quite straightforward to realise certain similarities between the torques provided by the spin-polarized current and the usual torques from the LLG equation. The first STT torque term, and the most relevant for STT-driven magnetization switching, is the so-called in-plane torque ($\Gamma_{\text{STT}}^{\text{IP}}$), since it lies in the plane defined by \mathbf{m} and \mathbf{m}_{RL} . This term is frequently designated by damping-like torque, since it has the same term dependency ($\mathbf{a} \times (\mathbf{a} \times \mathbf{b})$) as the damping torque in the LLG equation. The second STT torque term is labelled as field-like

torque ($\Gamma_{\text{STT}}^{\text{OOP}}$), due to its similarities to the precessional term in the LLG equation ($\mathbf{a} \times \mathbf{b}$). This term is usually small when compared to the damping-like and, regularly, neglected when designing a STT-MRAM [20, 39–42]. Finally, it is possible to write the full LLGS equation, taking into account only the damping-like torque

$$\begin{aligned} \frac{d\mathbf{m}_{\text{FL}}}{dt} = & -\gamma\mu_0\mathbf{m}_{\text{FL}} \times \mathbf{H}_{\text{eff}} - \alpha\gamma\mu_0\mathbf{m}_{\text{FL}} \times (\mathbf{m}_{\text{FL}} \times \mathbf{H}_{\text{eff}}) \\ & - \gamma\mu_0\eta_{\text{STT}} \frac{\hbar J}{2eM_s L} \mathbf{m}_{\text{FL}} \times (\mathbf{m}_{\text{FL}} \times \mathbf{m}_{\text{RL}}). \end{aligned} \quad (13)$$

Sometimes it is desirable to describe this effect taking into consideration an applied bias voltage V_{Bias} . One can do so, resorting to some modification of the equation (13) above

$$\frac{d\mathbf{m}_{\text{FL}}}{dt} = -\gamma\mu_0\mathbf{m}_{\text{FL}} \times \mathbf{H}_{\text{eff}} - \alpha\gamma\mu_0\mathbf{m}_{\text{FL}} \times (\mathbf{m}_{\text{FL}} \times \mathbf{H}_{\text{eff}}) - \gamma a_{\parallel} V_{\text{Bias}} \mathbf{m}_{\text{FL}} \times (\mathbf{m}_{\text{FL}} \times \mathbf{m}_{\text{RL}}). \quad (14)$$

with

$$a_{\parallel} = \frac{\hbar}{2e} \frac{\eta_{\text{STT}}}{\text{RA}} \frac{1}{M_s L} \quad (15)$$

using the following relation

$$J = \frac{V_{\text{Bias}}}{\text{RA}}, \quad (16)$$

where RA is the resistance-area product of the storage layer. The latter is highly dependent on the materials adjacent to the MgO tunnel barrier, as well as the oxidation time of this insulator layer. Analysing equation (13) it is possible to realise that the damping-like torque ($\Gamma_{\text{STT}}^{\text{IP}}$) can either reduce or enhance the effect of the damping torque, depending on the sign of the polarized-current. When $\Gamma_{\text{STT}}^{\text{IP}}$ opposes Γ_{damping} , and overcomes its value in magnitude, the amplitude of precession increases to the point where magnetization switching can occur (as depicted in figure 4 (b)). The current at which this phenomena occurs is denominated by critical switching current I_{c0} written for the macrospin case and at 0K [18, 20] as

$$I_{c0} = \frac{2e}{\hbar} \frac{\alpha}{\eta_{\text{STT}}} \mu_0 M_s A L H_{\text{eff}}. \quad (17)$$

It is important to realise that, since both magnetization in the free and pinned layer are perfectly collinear at 0 K, there is no reversal driven by STT, as there can not be any exerted torque on the magnetization of the free layer, $\mathbf{m}_{\text{FL}} \times \mathbf{m}_{\text{RL}} = 0$. In real cases, thermal fluctuations introduce an initial misalignment of \mathbf{m}_{FL} and \mathbf{m}_{RL} , promoting the torque to have a faster effect and, therefore, demand a smaller I_{c0} for the switching to occur. Moreover, as it can be seen, I_{c0} is proportional to H_{eff} . Thus, an IP or OOP configuration of the magnetization will yield different values of critical current, as can be seen for an expanded equation

$$I_{c0} = \frac{2e}{\hbar} \frac{\alpha}{\eta_{\text{STT}}} \mu_0 M_s A L [H_K + H_{\text{demag}}], \quad (18)$$

where, for further simplification, and assuming that the switching only occurs due to the effect of the spin-polarized current, we neglect contributions from H_{app} . For the case of an IP

magnetization, the dominating effect is the shape anisotropy, $H_{\text{demag}} \gg H_K$. This happens because, during the STT-induced switching, the magnetization has to precess OOP, resulting in a huge increase of the shape anisotropy contribution to the magnetic energy.

On the other hand, by stabilizing the magnetization in an OOP direction through the use of perpendicular anisotropy fields that overcome the effect of the shape anisotropy ($H_K > H_{\text{demag}}$), the memory cells can be patterned as flat cylinders ($H_{\text{demag}\parallel} \neq H_{\text{demag}\perp}$), allowing higher densities and a larger downsize scalability [20]. As a conclusion, a relation between Δ and I_{c0} can be extracted, as we are interested in memories with a high Δ , promoting a high retention time, and a low switching current I_{c0} .

As already mentioned in section 1.2, this stability factor is dependent on the operation temperature (T), and on the energy barrier (E_B) one must overcome to reverse the magnetization. Considering that this E_B is the sum of possible anisotropy energies, we can establish an effective anisotropy field (K_{eff}) which is related to the effective field H_{eff} :

$$H_{\text{eff}} = \frac{2K_{\text{eff}}}{\mu_0 M_s}. \quad (19)$$

Furthermore, knowing that the energy barrier is given by

$$E_B = K_{\text{eff}} V \quad (20)$$

we can rewrite

$$\Delta = \frac{\mu_0 M_s H_{\text{eff}} A L}{2k_B T}. \quad (21)$$

Finally, we are left with a proportional relation between I_{c0} and Δ

$$I_{c0} = \frac{4e \alpha k_B T}{\hbar \eta_{\text{STT}}} \Delta \quad (22)$$

as long as the macrospin approximation remains valid.

The relation Δ/I_{c0} is usually used as a figure of merit, known as the switching efficiency [20, 52]

$$\frac{\Delta}{I_{c0}} = \frac{\hbar \eta_{\text{STT}}}{4e \alpha k_B T}. \quad (23)$$

For a p-STT-MRAM this relation is larger than for an IP-STT-MRAM. However, this is only true as long as the damping does not grow larger. A solution to this problem appears when using only interfacial anisotropies for the anisotropy field, such as it is in the case of an FeCoB/MgO interface, as discussed before.

As already stated in the motivation for this thesis, section 1.3, there are still some limitations regarding the p-STT-MRAM. One of this limitations is the low Δ below 20 nm technological nodes. One of the proposed solutions is the novel PSA-STT-MRAM and, with the knowledge acquired in this chapter, we are able to understand the results obtained by Watanabe *et al.* [34] and Perrissin *et al.* [33]. For this purpose, the next section serves as a state of the art of the PSA-STT-MRAM.

3 Perpendicular shape anisotropy MRAM - a state of the art

As stated before, two different teams were successful in showing the novel concept of PSA-STT-MRAM [33,34]. They both reach the same conclusion, an increase of the thickness of the storage layer leads to a positive contribution of the shape anisotropy, enhancing the thermal stability factor and allowing an overcome of the downsize scalability limits of 20 nm of the p-STT-MRAM.

To introduce the evolution in thermal stability, we start by expanding the energy barrier taking into consideration the energy concepts of the last chapter:

$$\Delta = \frac{A}{k_B T} \left(\frac{1}{2} \mu_0 M_s^2 t (\mathcal{N}_{xx} - \mathcal{N}_{zz}) + K_s + K_u t \right) \quad (24)$$

where $\mathcal{N}_{xx} - \mathcal{N}_{zz} \approx -1$ for a p-STT-MRAM and t is the storage layer thickness. By modelling $(\mathcal{N}_{xx} - \mathcal{N}_{zz})$ it is possible to use the shape anisotropy as a positive contribution and enhance the energy barrier height, securing higher thermal stability factors. Moreover, an approximate expression for the demagnetizing factors can be used [33,53]

$$\mathcal{N}_{xx} - \mathcal{N}_{zz} = \frac{1}{2} \left(1 - \frac{3}{1 + \frac{4AR}{\sqrt{\pi}}} \right) \quad (25)$$

where AR is the aspect ratio of the storage layer, provided by the fraction of the thickness of the storage by its diameter t/D . In order to enhance the thickness of the storage layer, Perrissin [33] deposited a thick layer of cobalt (Co) on top of a conventional MTJ. The full stack is thus the following (thickness in nm): SiO₂ / Pt(25) / SAF / Ta(0.3) / FeCoB (1.1) / MgO(1.2) / FeCoB(1.4) (t^{SL}) / W(0.2) / TSL (t^{TSL}) / Ta (1) / Ru (10) / Ta (150). The synthetic antiferromagnetic layer (SAF) is made by (Co/Pt)₆/Ru/(Co/Pt)₃. This stack structure is used in conventional p-STT-MRAM, with the addition of a thick storage layer (TSL) on top of the existing FeCoB storage layer. The Pt (25) layer serves as a bottom electrode (needed to electrically connect the device), followed by an usual p-MTJ. This structure is made of the SAF, a multilayer composed by two ferromagnetic layers, antiferromagnetically coupled across a Ru spacer by the Ruderman-Kittel-Kasuya-Yoshida (RKKY) coupling [54,55]. This configuration reduces dipolar interactions between the electrodes. In addition, the usage of the SAF reduce the stray fields, leading to a symmetric switching, being one of the essential conditions for practical applications of the device [20,56]. Afterwards, we have the FeCoB reference layer, separated from the (Co/Pt)₃ pinned layer by a thin Ta layer. This spacer layer is inserted for an increase in iPMA and TMR, explained in more detail in the next chapter. Next we have the usual MgO tunnel barrier and the FeCoB storage layer. On top of this layer the TSL is deposited, enhancing the PMA with the strong effect of the shape anisotropy. The remaining of the top layer serves as a capping layer. The total thickness of the storage layer in equation (24) is the sum of the thickness of the FeCoB storage layer and the TSL, $t = t^{SL} + t^{TSL}$. Considering literature values for M_s and different anisotropic contributions, a diagram relating Δ , t and D is obtained, see figure 6. Moreover, for very

high AR a validity check of the macrospin approximation was performed, as the single domain particle approximation might no longer be valid [33]. For this purpose, minimum energy path (MEP) simulations using the string method were performed. These confirmed that, for some set of parameters (t, D), the switching mechanism is described by a nucleation and further propagation of a domain wall [33].

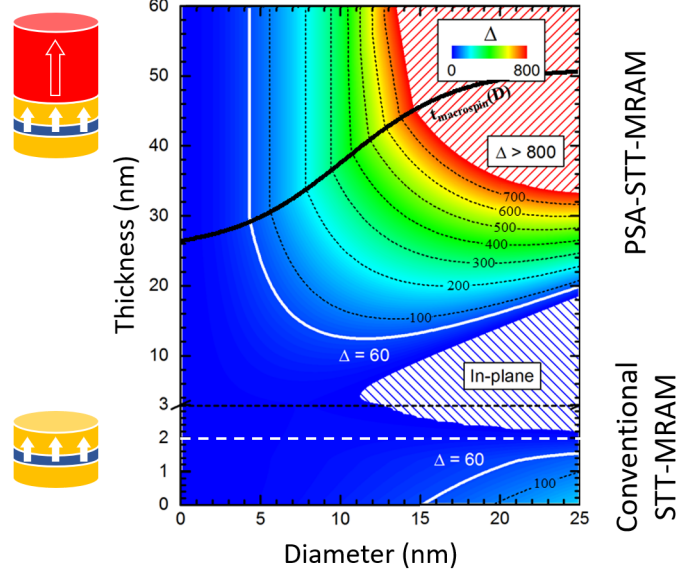


Figure 6: Stability diagram for a cylindrical storage layer, as a function of its total thickness (t) and Diameter (D). Values obtained at room temperature with literature values from [33]. The standard p-STT-MRAM encompasses $t < 3$ nm. Moreover, a thick black line is presented. The Δ values obtained after this line were done using micromagnetic simulations (MEP), as the switching mechanism is based on a domain wall nucleation and propagation. In the sketches, we see a usual p-STT-MRAM and the PSA-STT-MRAM, where the red thick storage layer is deposited. Figure adapted from [33]

Tohoku University was able, as well, to obtain working PSA-STT-MRAM devices. Their stack was, however, fairly different from the one used by Perrissin [34]. They used a structure made of a double Fe(B)/MgO interface, reaching a higher Δ (by a factor of 2) than a conventional p-STT-MRAM [57]. Doing so, a thinner storage layer was used (values near 15 nm). The loss of PSA is compensated by the second (capping) MgO layer, inducing an additional perpendicular orientation [20].

These different results pave the way towards sub-10 nm STT-MRAM based devices, promising to bring spintronic memory density one step closer to current microelectronic industry nodes. Nonetheless, for further optimization of these novel devices, studies on the switching mode reversal and improvements on the nanofabrication technique need to be made.

4 From idea to conception of a PSA-STT-MRAM cell

As stated before, the nanofabrication process of these structures is quite complicated, being one of the drawbacks of the technology. Moreover, in order to optimize it, we need to understand the way it is being done at the moment. For this purpose, we further divide this section in two parts. The first part is focused on the nanofabrication procedure of these novel PSA cells. With this objective, focus is given to different steps of the fabrication of the device. All these steps and procedures are made on the *Plateforme de Technologie Amount* (PTA) in Grenoble, by SPINTEC's MRAM group.

Moreover, due to the high aspect ratio of the patterned pillars, some of them might fall or tilt during the etching step. In order to correctly interpret the magnetoresistance loops, we must determine this possible angle of tilt. This information will give us the exact direction of the applied magnetic field with respect to the easy axis of our pillar. Thus, in the second part of this section, an experimental procedure based on the 3D Stoner-Wohlfarth astroid analysis is implemented, allowing the determination of the tilting angle of tilted pillars.

4.1 Nanofabrication process

The fabrication of a conventional MRAM takes into account a lot of different steps, starting from the deposition of the materials, the etching, and then several steps of lithography to end with a device that can be characterized electrically. Firstly the standardized method for a p-STT-MRAM is explained, exemplifying each of the phases with an associate diagram. The etching is seen in detail, as it is one of the most important stages, and the most difficult, when taking into consideration large memory densities, in the manufacturing of the cell.

Deposition and annealing

The layers were deposited by DC (Direct Current) and RF (Radio Frequency) magnetron sputtering on a thermally oxidized Si substrate. The MgO tunnel barrier is formed by exposing the RF-deposited Mg to an oxygen atmosphere. Afterwards, the stack is annealed. Starting from the as-deposited stack, amorphous layers of FeCo(B) are atop a polycrystalline MgO tunnel barrier. The annealing step is thus a necessity to ensure a coherent crystallization of FeCo with MgO grains and ensure the formation of Fe-O orbital hybridization that is at the origin of the iPMA [44]. During the crystallization of the FeCo, the excessive boron is segregated to grain boundaries and interfaces and, for that reason, a Ta layer is deposited adjacent to the FeCoB due to its role as a B getter. This will absorb the B away from the FeCo / MgO interface, ensuring a good crystallization and, consequently, improving the TMR. A lateral patterning is then carried out after the deposition and annealing of the multilayer in order to fabricate the high-aspect ratio PSA pillar.

In order to explain the patterning process, we start with the exemplified stack, composed of the SiO₂ substrate (black color), the bottom electrode (brown color), the SAF and reference layer (green), the MgO tunnel barrier (yellow color), the total storage layer (red color) and,

finally, the Ta hard-mask (with a grey color), figure 7 a). In the first step, a negative resist is deposited on top of the deposited stack. Afterwards, an electron beam (e-beam) is used to remove the resist at the desired location of the pillars, exposing the Ta hard mask, figure 7 b). Then, a Cr layer is deposited by evaporation, filling the holes left in the resist, figure 7 c). Afterwards, the resist is removed resorting to a chemical treatment, figure 7 d). Since we now have the desired location of the pillar, we can define the Ta hard mask. This is done by using Ta selective (it will only remove Ta) reactive ion etching (RIE), stopping at the Ru layer right below the hard mask. Since this step is done perfectly vertically to the stack, the Ta that is underneath the Cr is protected, resulting in a well defined Ta hard mask, see figure 7 e).

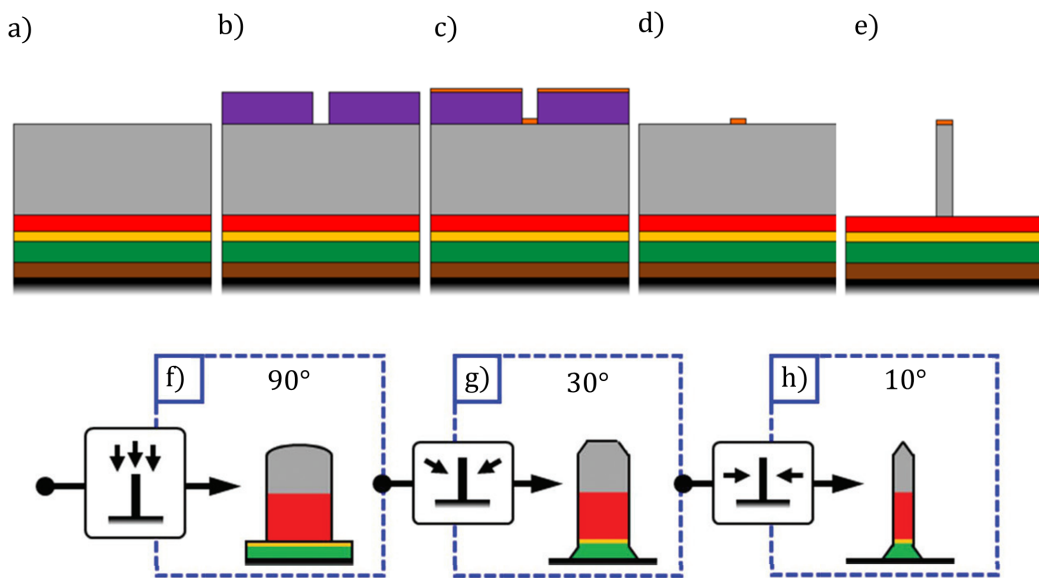


Figure 7: Steps on the definition of the Ta Hard Mask (a - e) and of the MTJ pillar (g-h). Figures adapted from [58].

The MTJ pillar is defined, after the hard mask has been prepared, using ion beam etching (IBE) in three different steps, where the angle of the beam relative to the pillar is modified. The procedure exemplified here is the one being used for the PSA cells and adopted by Perrisin [33].

In the first step, the beam angle is set at a normal incidence, figure 7 f). In this step, the main etched structure is the storage layer. As the free particles of the etched materials are quite susceptible to redeposition, the diameter of the pillar will increase. This etching step is performed until the MgO layer is reached. It is important to stop there, since some of the etched material offers a higher conductivity than the MgO tunnel barrier. Thus, redeposition would lead to short-circuits along the barrier (shunts).

The second step starts with a modification of the etching angle at 30°, as seen in figure 7 g). This angle ensures that the etching rate is higher than the redeposition rate [33], avoiding shunts. This second steps gives a conical shape to the SAF, which does not affect

the performance of the device, as long as the storage layer is cylindrical. The third step begins after the bottom electrode is reached, meaning that all the stack is now etched. However, as stated before, the diameter of the pillar is larger than it should be, due to the redeposition. In order to ensure the desired final diameter of the pillar, a last step is performed. This consists of a lateral etching, with a grazing angle of 10° (figure 7 h)). This step will allow to trim the pillars until the desired diameter is reached.

Defining the top and bottom electrodes

The designing of the electrodes starts with the definition of the bottom electrode. This step is realised by using ultra-violet (UV) lithography, where first a photo resist (represented with a purple color) is spread on the wafer, and insulated at some particular locations where we want to keep the resist. After a chemical treatment, only the insulated resist is removed to obtain the result illustrated in figure 8 a). Then, using selective RIE, the Pt bottom electrode is etched everywhere, except at the place where the photo-resist is placed, as shown in figure 8 b). The hole etched by RIE, in the Pt layer, on the right part of the pillars, is done to dissociate the bottom and future top contacts of the pillars, preventing the contact between neighbouring pillars. The Pt underneath the pillars is the bottom electrode, and the Pt on the right side of the hole is the future top electrode. Finally, the resist is chemically removed, figure 8 c).

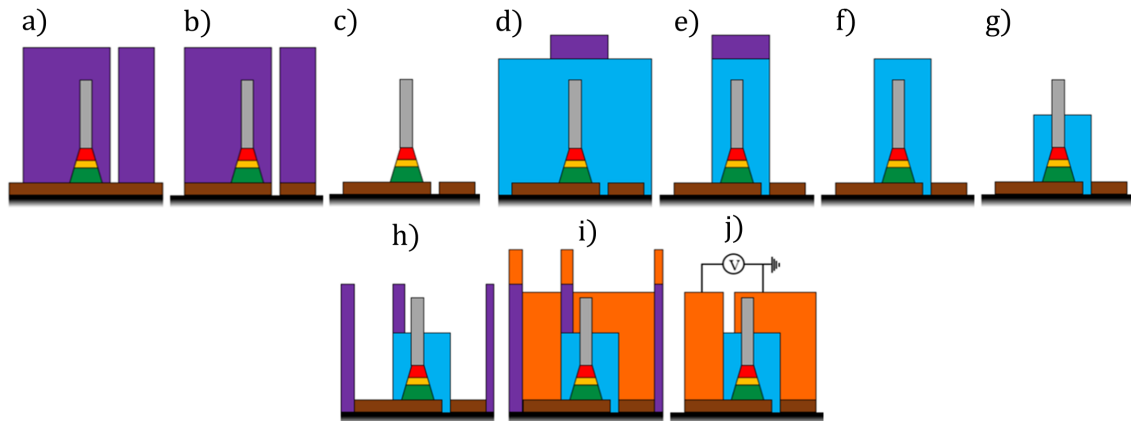


Figure 8: Schemes of the steps for defining the bottom (a-c) and top (d-g) electrodes and the electric contacts (h-j). Figure adapted from [58].

After the bottom electrode is defined, the pillar is encapsulated with accuflo, a dielectric isolator, represented with a blue color in figure 8 d). Using another lithography step, the resist is placed in such a way, that it covers the top of the pillar and the hole etched by RIE, separating the bottom and the future top electrodes, figure 8 d). The unnecessary accuflo is then removed with selective RIE, figure 8 e). This step exposes the top and bottom electrodes in order to allow them to be electrically connected. The resist is afterwards removed with

a chemical treatment, figure 8 f). In order to realise the top contact, we need to reveal the top of the pillar (*i.e.* the Ta hard mask). This is done by thinning the accufflo in such a way that, at the end, only half of the Ta hard mask is outside of the accufflo, figure 8 g). Now, it is possible to define the electric contacts. For this part, we use a last step of the UV lithography, in which we first deposit a resist that we insulate at certain locations. The insulated resist is then removed to obtain the result shown in figure 8 h). Afterwards, a layer of Cr (10 nm), and Al (300 nm) is deposited by evaporation as conductive top and bottom electrodes. The resist still present from the previous lithography step prevents to have any shorts between top and bottom contacts, figure 8 i). Then, as the resist is washed away, we can electrically connect the electrodes, figure 8 j).

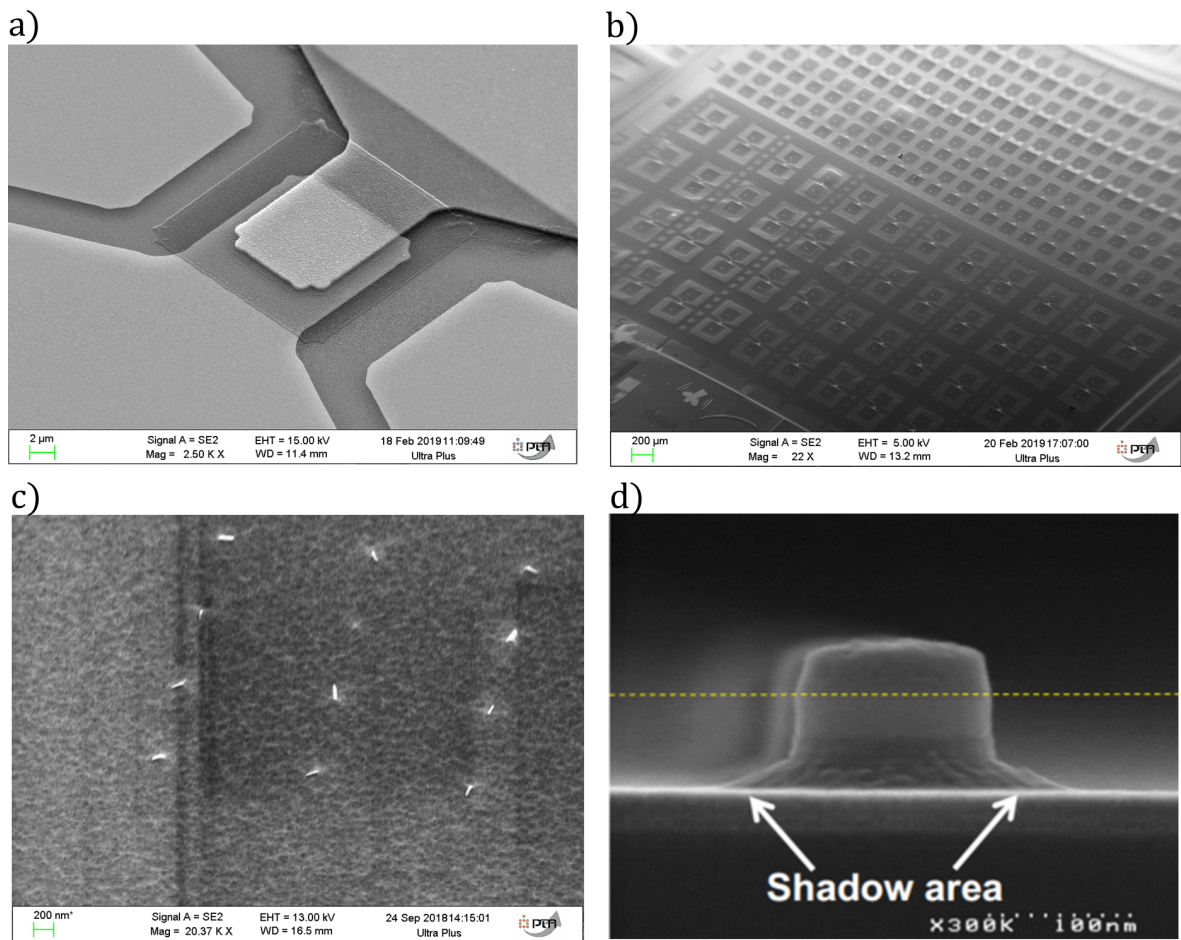


Figure 9: (a) Example of a final device, after the definition of the top and bottom electrodes. The pillar is unseen but it sits on the middle of the device. Scale of 2 μm (b) Full array of PSA-STT-MRAM, showing the density of the final device. Scale of 200 μm. (c) Example of pillars before the electrodes are defined. We can observe straight, tilted and fallen pillars. Scale of 200 nm. SEM images obtained by the SPINTEC MRAM group at the PTA, Grenoble France. (d) Shadow effect originated from the etching step, promoting a decrease of the density of pillars in the device. Scale of 100 nm. Image extracted from [59].

In figure 9, scanning electron microscope (SEM) images of the device after the final

fabrication step are shown. The top and bottom electrode pads are clearly seen in figure 9 a) as well as the accufflo ensuring electric isolation of the pillar. Figure 9 b) shows a full array of pillars. Although this nanofabrication process proves a viable solution for the production of sub-10 nm pillars with a very high AR, some aspects need to be studied and improved. Besides the possible formation of shunts during the patterning, the shadow effect, typical of the ion beam-etching step promotes the appearance of a footing (see figure 9 d)). Such a shadow effect must be addressed, as it compromises the density of pillars that can be achieved in the array. In addition, the high AR of the patterned pillars yields a significant variability in the fabrication process, in particular due to some fallen and tilted pillars (see figure 9 c)). A model based on the 3D Stoner Wohlfarth theory was developed to readily determine the tilting of the pillar. That model is explained in detail in the next section and it may be employed for the assessment of the tilting of the pillars resulting from the deposition process described above.

4.2 Determination of pillar tilt angle from 3D Stoner Wohlfarth astroid analysis

To study the electrical properties of the PSA-STT-MRAM cells, the magnetic field is usually applied perpendicular to the wafer plane. This is supposed to correspond to the easy axis of magnetization, assuming the pillar is perfectly perpendicular to the plane of the wafer. However, if the pillar is tilted, this direction is misaligned from the pillar axis by a certain angle. To avoid misinterpreting magnetoresistance data, it is therefore highly desirable to be able to detect the presence of any pillar tilt and quantify it. For this purpose, we have developed a methodology to determine a possible pillar tilt based on the 3D Stoner-Wohlfarth model. This method mitigates the need for a high-field 3D vector magnet for identifying the pillar orientation, instead requiring only anisotropy measurements along two polar axis.

The experimental results which illustrate this section were obtained by Nicolas Perrissin, from the MRAM group, SPINTEC, for a 13 nm diameter cylindrical pillar. The fabrication of this element was realised by the MRAM group at the PTA, using the different nanofabrication steps presented in the last subsection. The pillar has the following stack structure (thickness in nm): SiO₂ / Pt(25) / SAF / Ta(0.3) / FeCoB(1.1) / MgO(1.2) / FeCoB(1.4) / Ta(0.2) / Co(60) / Ta(1) / Ru(10) / Ta(150). The Synthetic Antiferromagnet (SAF) layer was composed of (Co/Pt)₄ / Ru(0.8) / (Co/Pt)₃. Figure 10 shows an example of a set of magnetoresistance loops measured at different angles of applied field (\mathbf{H}) with respect to the plane of the wafer. A tilt of the pillar axis can already be detected from these curves. Indeed, for a 90° orientation, corresponding to a field parallel to the plane of the wafer (black line), the shape of the curve should exhibit a reversible hard-axis behaviour, which is not the case. Also, for a 0° orientation (red line), the loop should be square, whereas the resistance does vary on the upper and lower branches of the hysteresis loops. To get further insight into this misalignment, we can extract the angular dependence of the coercive field (H_{coercive}) from the measurements of the R(H) cycles. In a macrospin approximation, this dependency

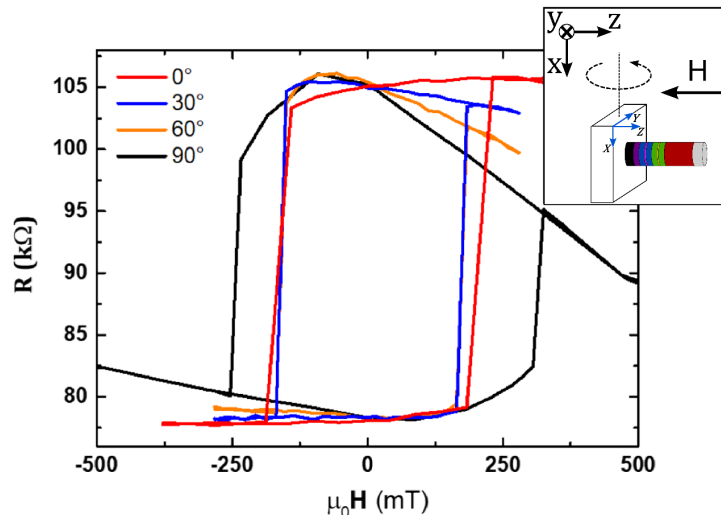


Figure 10: Evolution of the resistance (R) as a function of \mathbf{H} for different field orientations (90° =field applied in the wafer plane, 0° =field applied normal to the wafer plane). The lines in red and black represent the cases where the field is applied orthogonal to the wafer plane (0° , i.e. along the expected easy axis if the pillar was perfectly perpendicular to the wafer) and parallel to the wafer plane (90° , i.e. along the expected hard plane if the pillar was perfectly perpendicular to the wafer), respectively. Inset: schematic representation of the experiment and frames from the laboratory (black) and wafer (blue). In this sketch, the PSA-STT pillar is assumed to be perfectly perpendicular to the wafer plane. Experimental results obtained by Nicolas Perrissin.

can be analysed using the Stoner-Wohlfarth model. However, for the studied storage layer shape (very thick layer), the expected switching mechanism is based on domain wall nucleation/propagation [14]. Nonetheless, the magnetization switching for a field applied along the hard axis of the cell can still be considered as a coherent reversal, as long as the condition $D < 4\lambda_{\text{ex}}$, where D is the pillar diameter and λ_{ex} the exchange length, is fulfilled [60]. The Stoner-Wohlfarth model is used to describe the coherent reversal of a uniformly magnetized ellipsoid [61]. Its analysis leads to the well-known Stoner-Wohlfarth astroïd. Using it, the angular dependence of H_{coercive} can be modelled by the relation

$$\frac{H_{\text{coercive}}(\xi)}{H_{\text{coercive}}(\xi=0^\circ)} = \left[\sin^{\frac{2}{3}}(\xi) + \cos^{\frac{2}{3}}(\xi) \right]^{-\frac{3}{2}} \quad (26)$$

where ξ is the angle between \mathbf{H} and the easy axis of the pillar [61,62]. In the case of our cylindrical pillars (figure 11 a)) we need to extend the conventional 2D Stoner-Wohlfarth model to 3D [63,64]. The 2D astroïd is then converted into a revolution astroïd, as shown in figure 11 c). It is characterized by an easy axis along the pillar axis and a hard plane parallel to the layer plane. Since the direction vectors of this astroïd are orthonormal: $\mathbf{k}_{\perp 1} \perp \mathbf{k}_{\perp 2} \perp \mathbf{k}_{\parallel}$, the identification of two hard-axes of the pillar enables the characterization of its easy axis and, therefore, of its tilt angle. Any hard axis direction within the hard plane shows up in the $R(H)$ experiments, as in figure 10, as a maximum of coercivity. To find

two hard-axis directions, two sets of $R(H)$ curves versus angle between \mathbf{H} and the substrate holder were measured for two orthogonal orientations of the sample holder, as seen in figure 12. For further analysis, we define a frame $(\mathbf{X}, \mathbf{Y}, \mathbf{Z})$ attached to the wafer/substrate holder as represented in figure 11 b). The X and Y axes are in the plane of the wafer and Z is orthogonal to it. In the first measurement (figure 12 a)) the sample holder rotates in the

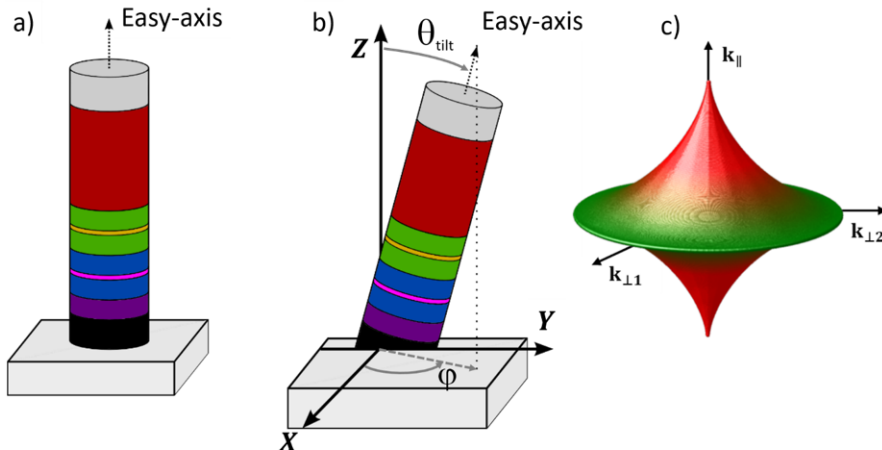


Figure 11: Schematic representation of the studied PSA-STT pillars. The thick Co (60 nm) layer is represented by the red color. (a) Representation of the pillar with its easy axis of magnetization aligned along the pillar axis. (b) Representation of a tilted pillar, the tilt is characterized by the tilt angle θ_{tilt} and azimuthal angle φ . The X and Y axes are in the plane of the wafer. (c) 3D Stoner Wohlfarth astroid with revolution symmetry describing the switching field of the storage layer magnetization. The \mathbf{k}_{\parallel} direction corresponds to the easy-axis direction whereas $\mathbf{k}_{\perp 1}$ and $\mathbf{k}_{\perp 2}$ lie in the hard-plane.

electromagnet gap (lab frame) around the X -axis, meaning that the applied field in the frame of the sample is rotating in the YZ -plane. In contrast, in the second configuration (figure 12 b)), the sample rotates around the Z -axis in the lab frame, so that the field rotates in the XY -plane of the sample frame. From the values of coercivity, corresponding to situations where the applied field lies in the hard plane of magnetization, it is possible to obtain two different angles, ($\theta_{\perp 1}$ and $\theta_{\perp 2}$) and their corresponding vectorial directions $\mathbf{k}_{\perp 1}$ and $\mathbf{k}_{\perp 2}$, at which a hard-axis behaviour is observed. The pillar axis direction is then along the $\mathbf{k}_{\perp 1} \times \mathbf{k}_{\perp 2}$ direction. The pillar anisotropy field can also be derived from the maximum value of the coercive field obtained when the applied field lies in the hard plane. This anisotropy field corresponds to $H_{\text{coercive}}(\xi = 0)$ in equation (26). These values of H_{coercive} are calculated from the RH curves as the field where we have a normalized resistance of 0.5. This means that half of the storage layer is already switched. However, this method is only valid for the case where we have a hysteresis loop. As expected, when we apply the field along a hard axis, there is no hysteresis loop and, consequently, the field necessary to switch half of the storage layer is, theoretically, considered infinite.

Experimentally, this hard-axis behaviour is observed by doing an angular dependence of \mathbf{H} and verified when the hysteresis loop disappears. This can be observed in figure 13, where,

for the first configuration, we are unable to calculate a value of coercive field for an angle of 95° and, by symmetry, at -85° , as shown figure 13 a). In the second configuration, we have a higher dispersion of angles where a lack of hysteresis exist. Since they are around the central value of 40° , we select this value and establish an error of 10° , associated with the width of the red stripes. This can be seen in figure 13 b). This uncertainty can be, afterwards, used as an error in the angle and, by error expansion in the following equations, used to calculate an experimental error associated with the obtained tilting angle. We further observe that this error is not significant and is, therefore, neglected in this discussion. In order

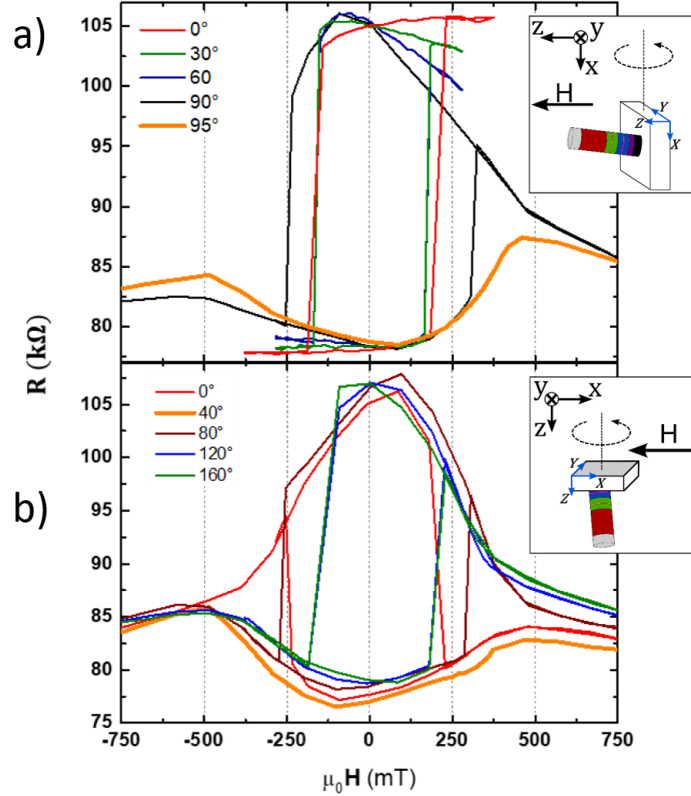


Figure 12: Magneto-resistance loops as a function of \mathbf{H} for different orientation angles of the pillar axis. The insets represent sketch of the two experimental geometries. In the first configuration (a) the wafer rotation axis is the x-axis and the field is applied in the YZ plane. The maximum coercivity corresponding to \mathbf{H} within the hard plane is observed for an angle of $\theta_{\perp 1} = 95^\circ$. In the second configuration (b), the wafer rotation axis is the z-axis, and the field is applied in the XY plane. \mathbf{H} lies within the hard plane for $\theta_{\perp 2} = 40^\circ$. Experimental results obtained by Nicolas Perrissin.

to quantitatively interpret the experimental results, we then first simulated the $R(H)$ loops of the junction in the macrospin regime for different field orientations, deriving from those the variation of H_{coercive} for the different angles, figure 13 (green points). For this purpose, we use a three layer macrospin model approximation, composed of the free-layer and the bottom- and top-part of the SAF. Since we want to extract H_{coercive} from the RH curves, one should

know the orientation of both the magnetization in the free- and pinned-layer. Therefore we start with the energy model of the free-layer

$$E_{\text{FL}} = E_{\text{exchange}} + E_{\text{K}} + E_{\text{demag}} + (E_{\text{dip}}^{\text{TSAF}} + E_{\text{dip}}^{\text{BSAF}}) + E_{\text{Z}}, \quad (27)$$

where E_{exchange} is the exchange energy, E_{K} the perpendicular anisotropy energy, E_{demag} the demagnetizing energy, related with the effect of the shape anisotropy, E_{Z} the Zeeman energy, from the interaction between the magnetization and \mathbf{H} and $(E_{\text{dip}}^{\text{TSAF}} + E_{\text{dip}}^{\text{BSAF}})$ the contribution from the dipolar field from the top- and bottom-part of the SAF. Experimentally, the effect of the latter is very small and, for further simplification, neglected in the simulation. As

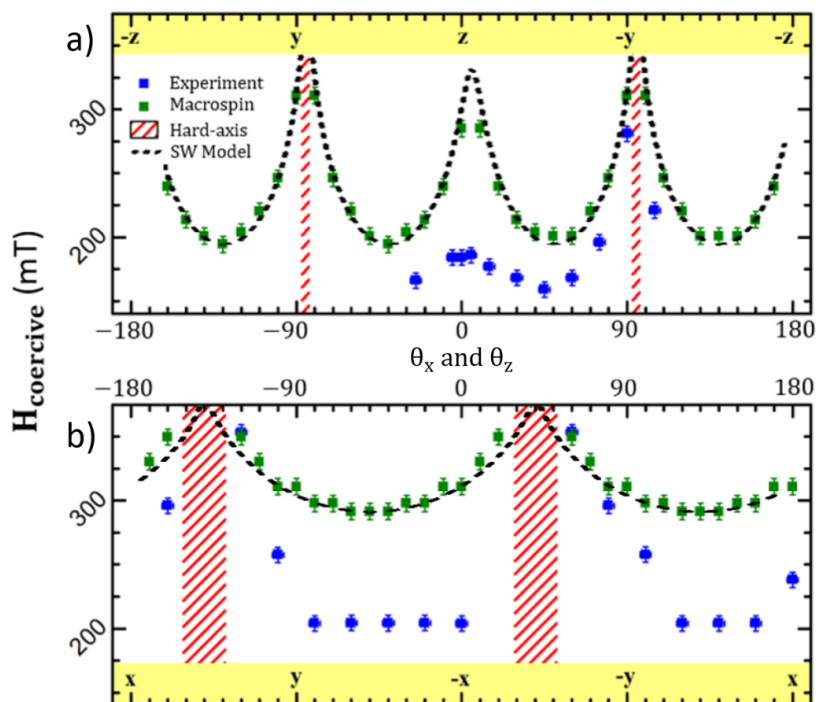


Figure 13: Angular dependence of the two experimental situations of figure 12: (a) the wafer rotation axis is the x-axis and the field is applied in the YZ plane. (b) The wafer rotation axis is the z-axis and the field is applied in the XY plane. The blue squares represent the experimental results. The maximum coercivity H_{coercive} corresponding to a field applied in the hard-plane is marked with red stripes, the width of which corresponds to the experimental uncertainty. The green squares represent the coercivity values derived from a macrospin simulation of the hysteresis loops. Dashed black line: analytical variations derived from the 3D Stoner-Wohlfarth model.

we require the knowledge of the equilibrium angle of the magnetization for different field orientations, the total energy needs to be minimized. This model can be further simplified knowing that, in a macrospin regime, the different spins are aligned, conferring a constant value to the exchange energy. Thus, this value is discarded from the energy minimization. After calculating the equilibrium angle of the magnetization for different angle orientations, one might deduce the relative resistance for each \mathbf{H} orientation. Admitting that the reference

layer magnetization is fixed, it is only necessary to calculate the angle of the magnetization in the free layer of Co (60 nm).

For each equilibrium angle and, working with a normalized resistance, where the minimum resistance is given when both magnetizations are aligned ($R_P = 0$, for $\theta = 0$), it is possible to calculate the associated resistance for each angular orientation as

$$R(\theta) = R_P + \frac{\Delta R}{2}(1 - \cos \theta) \quad (28)$$

where R_P is the resistance for a parallel state, $\Delta R = R_{AP} - R_P$, with R_{AP} the maximum resistance, associated with an anti-parallel state [51]

As expected, when the field is close to the hard-plane, the experimental coercivity, figure 13 (blue points), variation is close to the simulated one since the switching mechanism is a coherent rotation. In contrast, away from the hard-plane, the experimental coercivity is much reduced compared to the macrospin calculated one due to magnetization reversal by domain wall nucleation/propagation for this very thick storage layer.

We further checked that the results of the macrospin simulations were in accordance with equation (26). For this purpose, we need to express the angle ξ as a function of the parameters characterizing the geometry of the measurements *i.e.* θ_{tilt} and φ characterizing the pillar tilt and tilt azimuth, as well as θ_x and θ_z characterizing the rotation of the substrate with respect to the field in the two experiments depicted in figures 12 a) and 12 b).

The angle ξ is given by

$$\cos \xi = \mathbf{k}_{\parallel} \cdot \mathbf{H} \quad (29)$$

where \mathbf{k}_{\parallel} is the unit vector along the easy-axis of our PSA pillar (*i.e.* the pillar axis itself). This can be expressed as the unit vector along the pillar axis in the frame of the wafer. Using the notion of figure 11 b), \mathbf{k}_{\parallel} is given by:

$$\mathbf{k}_{\parallel} = \sin \theta_{\text{tilt}} \cos \varphi \mathbf{X} + \sin \theta_{\text{tilt}} \sin \varphi \mathbf{Y} + \cos \theta_{\text{tilt}} \mathbf{Z}. \quad (30)$$

For each orientation of the sample holder during its rotation, the new orientation of the pillar axis is characterized by the new vector $\mathbf{k}_{\parallel}^{\text{rot1(2)}}$ which can then be derived using a transformation associated with the rotation around the axis of rotation. The superscript 1 or 2 refers respectively to the first and second measurement configuration of the substrate holder. This new vector is defined as

$$\mathbf{k}_{\parallel}^{\text{rot1}} = R_x(\theta_x) \mathbf{k}_{\parallel} \quad (31)$$

for the case where \mathbf{H} is applied in the YZ plane (1st configuration), and

$$\mathbf{k}_{\parallel}^{\text{rot2}} = R_z(\theta_z) \mathbf{k}_{\parallel} \quad (32)$$

for the case where \mathbf{H} is applied in the XY plane (2nd configuration). The angles θ_x and θ_z represent the rotation angles around the x- and z-axis, respectively. The ξ angle can then be

calculated as:

$$\begin{aligned}\cos \xi &= \mathbf{k}_{\parallel}^{\text{rot1}} \cdot \frac{\mathbf{H}}{|\mathbf{H}|} \\ &= \cos \theta_x \sin \theta_{\text{tilt}} \sin \varphi + \cos \theta_x \cos \theta_{\text{tilt}}\end{aligned}\quad (33)$$

for the first configuration, and

$$\begin{aligned}\cos \xi &= \mathbf{k}_{\parallel}^{\text{rot2}} \cdot \frac{\mathbf{H}}{|\mathbf{H}|} \\ &= \cos \theta_z \sin \theta_{\text{tilt}} \cos \varphi - \sin \theta_z \sin \theta_{\text{tilt}} \sin \varphi\end{aligned}\quad (34)$$

for the second measurement configuration.

With these expressions, equation (26) and the values of θ_{tilt} and φ , we can plot the theoretical angular dependencies of H_{coercive} resulting from the Stoner-Wohlfarth model (figure 13, dashed black line). From this figure, two important conclusions can be drawn. Near the hard plane, the reversal process can be considered as macrospin as previously discussed. However, this does not hold for other orientations. As can be seen, for both measurement geometries, the experimental values away from the hard-plane are significantly lower than the ones expected from the simulation, even though they are following the same angular trend. This indicates that the magnetization reversal process occurs then by nucleation/propagation of domain walls. In addition, two direction vectors, characterizing the two determined hard axes, $\mathbf{k}_{\perp 1}$ and $\mathbf{k}_{\perp 2}$, can be derived and expressed in Cartesian coordinates in the frame of the sample holder:

$$\mathbf{k}_{\perp 1} = \begin{pmatrix} 0 \\ -\sin 95^\circ \\ \cos 95^\circ \end{pmatrix} \quad \text{and} \quad \mathbf{k}_{\perp 2} = \begin{pmatrix} \cos 40^\circ \\ \sin 40^\circ \\ 0 \end{pmatrix}. \quad (35)$$

Knowing that the easy axis is simply given by the vector product of these two direction vectors, it is possible to obtain the tilt angle of our PSA cell from $\mathbf{k}_{\parallel} = \frac{\mathbf{k}_{\perp 1} \times \mathbf{k}_{\perp 2}}{\|\mathbf{k}_{\perp 1} \times \mathbf{k}_{\perp 2}\|}$, yielding a value of $\theta_{\text{tilt}} = 6.5^\circ$ and $\varphi = 50^\circ$.

5 Micromagnetic analysis of the PSA-STT-MRAM

As stated in section 3, the most probable energy path between two stable states of the magnetization evolves from macrospin-like behaviour to a domain wall (DW) propagation for a certain thickness threshold [33]. As the storage layer thickness is affecting its thermal stability factor and the writing operation of the cell, a knowledge of the physical phenomena happening during the magnetization reversal driven by STT is important for the engineering of optimized devices. For this purpose, the mechanism of magnetization reversal during the writing operation for the PSA-STT-MRAM induced by STT is carried out using micromagnetic simulations.

5.1 Micromagnetic model

In most simple cases, a magnetic problem can be solved in the framework of macrospin approximation. However, in real samples, the volume of the magnetic body is divided in magnetic domains, separated by magnetic domain walls (discussed in subsection 2.2). Thus, when solving realistic cases, these different concepts must be taken into account.

Furthermore, as each magnetic domain has a defined magnetization, the local magnetization of the system is described as a continuous function, dependent on the position \mathbf{r} and time t

$$\mathbf{M}(\mathbf{r}, t) = M_s \mathbf{m}(\mathbf{r}, t), \quad (36)$$

where \mathbf{m} is the unitary vector defining \mathbf{M} with a saturation magnetization M_s . This formalism is the first step towards the micromagnetic description of a magnetic body.

Moreover, the different interactions acting on the magnetic system will lead it to different equilibrium magnetization arrangements. Taking these different interactions into consideration, the micromagnetic theory allows to forecast the temporal evolution of the configuration of the magnetization of the magnetic body [20, 65]. For this purpose, the different energy terms presented in section 2 are rewritten, taking into consideration the assumptions made before.

In this model, the exchange energy is considered, as the different neighbouring spins can be misaligned, being minimized for a parallel arrangement. As this interaction is a short-range one, only neighbouring spins are accounted for. Furthermore, treating small deviations between spin alignments with equal quantum spin operator \mathbf{S} , the scalar product of equation (10) can be reduced to

$$\mathbf{S}_i \cdot \mathbf{S}_j = S^2 \left(1 - \frac{1}{2} [(\mathbf{r}_{ij} \cdot \nabla) \mathbf{m}(\mathbf{r}_{ri})]^2 \right). \quad (37)$$

As the micromagnetic theory has a continuous description, the exchange energy is expressed as

$$E_{\text{exchange}} = \int_V A_{\text{ex}} ([\nabla m_x(\mathbf{r})]^2 + [\nabla m_y(\mathbf{r})]^2 + [\nabla m_z(\mathbf{r})]^2) d\mathbf{r} \quad (38)$$

where A_{ex} is the exchange stiffness constant, attained considering that the exchange coupling

is constant throughout the entire magnetic body [20].

The different magnetocrystalline anisotropies (such as PMA and iPMA) are expressed as

$$E_{\text{uniaxial}} = \int_V K_u (1 - [\mathbf{u}_k \cdot \mathbf{m}(\mathbf{r}, \mathbf{t})]^2) d\mathbf{r}, \quad (39)$$

where \mathbf{u}_k is the unit vector parallel to the easy axis of the material and K_u an uniaxial anisotropy energy constant.

The shape anisotropy energy follows the same principle,

$$E_{\text{shape}} = -\frac{1}{2} M_s \mu_0 \int_V \mathbf{m}(\mathbf{r}, \mathbf{t}) \cdot \mathbf{H}_{\text{demag}}(\mathbf{r}, \mathbf{t}) d\mathbf{r}. \quad (40)$$

It should be noted that these expressions differ from the macrospin regime due to their space dependency. As for the case of the energy resulting from an interaction of the applied magnetic field $\mathbf{H}_{\text{applied}}$ and the magnetization \mathbf{M} in the body (Zeeman energy), it is given as

$$E_{\text{Zeeman}} = -\mu_0 M_s \int_V \mathbf{m}(\mathbf{r}, \mathbf{t}) \cdot \mathbf{H}_{\text{applied}}(\mathbf{r}, \mathbf{t}) d\mathbf{r} \quad (41)$$

considering that $\mathbf{H}_{\text{applied}}$ can be time dependent.

In addition, it is possible to express the effective magnetic field \mathbf{H}_{eff} as a function of the variational derivative of the Gibbs free energy density ε_{tot} :

$$\mathbf{H}_{\text{eff}} = -\frac{1}{\mu_0 M_s} \frac{\delta \varepsilon_{\text{tot}}}{\delta \mathbf{m}}, \quad (42)$$

where the total energy of the magnetic system is given by

$$E_{\text{tot}} = \int_V \varepsilon_{\text{tot}} dV. \quad (43)$$

Thus, \mathbf{H}_{eff} can be written as

$$\mathbf{H}_{\text{eff}} = \frac{2A_{\text{ex}}}{\mu_0 M_s} \nabla^2 \mathbf{m} + \frac{2K_u}{\mu_0 M_s} (\mathbf{u}_k \cdot \mathbf{m}) \mathbf{u}_k + \mathbf{H}_{\text{app}} + \mathbf{H}_{\text{demag}} \quad (44)$$

for a sample with uniaxial anisotropy.

With these results, it is possible to calculate the equilibrium state of the magnetization [20]. Nonetheless, as we are interested in understanding the dynamical behaviour of the magnetization during the switching process, the LLGS equation of motion, described in section 2, is implemented in the micromagnetic framework. For this purpose, a mesh size is defined, where \mathbf{H}_{eff} is calculated for each elementary unit of the mesh, defined as the cell. Obviously, by varying the size of this cell element, the accuracy of the result will be different, improving as the cell size decreases. However, this brings a heavier computational burden, taking longer time to compute. Thus, it is important to know what is the maximum cell size we can use. This parameter is defined by relating the magnitude of the exchange interaction with the remaining anisotropic contributions, as it has the shortest interaction range,

determining the typical scale at which the magnetization can vary. From this assumption, two different length scales are defined, the exchange length λ_{ex} and the Bloch length λ_{B} , respectively

$$\lambda_{\text{ex}} = \sqrt{\frac{2A_{\text{ex}}}{\mu_0 M_{\text{s}}^2}} \quad (45)$$

and

$$\lambda_{\text{B}} = \sqrt{\frac{A_{\text{ex}}}{K_{\text{u}}}}. \quad (46)$$

As it can be seen, λ_{ex} reflects the competition between the exchange interaction and the effect of the shape anisotropy. On other hand, λ_{B} results from the relative strength of the exchange interaction and the uniaxial anisotropy. The selected cell size must be smaller than both these lengths for a accurate description of the effect of neighbouring magnetic moments.

5.2 Magnetization reversal in PSA-STT-MRAM

In this micromagnetic study, we are interested in discovering the reversal mechanism behind the magnetization switching in a PSA-STT-MRAM. For this purpose, a dynamical study based on the LLGS equation is made. This investigation is performed using a micromagnetic solver developed by Liliana Buda Prejbeanu, a researcher at SPINTEC. Furthermore, as the resolution of these simulations is demanding, an implementation in the GPU architecture is performed, leading to a faster processing. The object of study are thick FeCoB storage layers, with a diameter of 20 nm and different thicknesses, figure 14 a). The material is assumed to posses $M_{\text{s}} = 1 \times 10^6$ A/m, A_{ex} of 1.5×10^{-11} J/m and a damping value α of 0.01 [20]. Using these values and equation (45), a value of $\lambda_{\text{ex}} \approx 5$ nm and $\lambda_{\text{B}} \approx 4.4$ nm is obtained. Based on these results, a cell of size of 2 nm can be used. Since these mesh elements are cubic shaped, a squared pillar format is used, instead of circular, as a reliable result would be only obtained for very small cell size. Furthermore, as in our device the source of iPMA comes from the FeCoB/MgO interface, this effect is implemented by adding an evanescent uniaxial contribution to our system.

The equilibrium state is calculated for each simulation, where a modification of AR, cell size or intrinsic material parameters happens. For this purpose, we allow the magnetization to reach its equilibrium state by setting a high value of α . When the total energy stabilizes (does not vary in time), it reaches a local minimum, and we consider this magnetization configuration as the initial step for our upcoming dynamical simulations. From this point forward, external contributions can be added in our system. This is the case of a current polarized in spin or an applied magnetic field. In figure 14, a comparison between the equilibrium initial state of the magnetic pillar with and without the effect of the uniaxial anisotropy is shown. From figure 14 b), a misalignment near the top and bottom surface in the magnetization along the pillar axis direction (defined as the \mathbf{z} axis), is observed. This effect is quite symmetrical in figure 14 b) (left side), as we only have the effect of the shape anisotropy inducing a perpendicular orientation. However, when introducing an iPMA from

the FeCoB/MgO interface, a sturdier perpendicular orientation of the magnetization is enforced. Thus, the magnetic moments near the bottom surface will follow this preferential alignment, figure 14 b) (right side). In addition, since this uniaxial anisotropy is originated at the interface, it only acts on the first layer of cells. Therefore, the top-surface magnetic display is similar to the one without the influence of K_u . A 3D display of the magnetization along the symmetry axis of the pillar (M_z) for both these situations is displayed in figure 14 c), where the magnetization for each cell element is displayed as an arrow, demonstrating the misalignment of some magnetic moments.

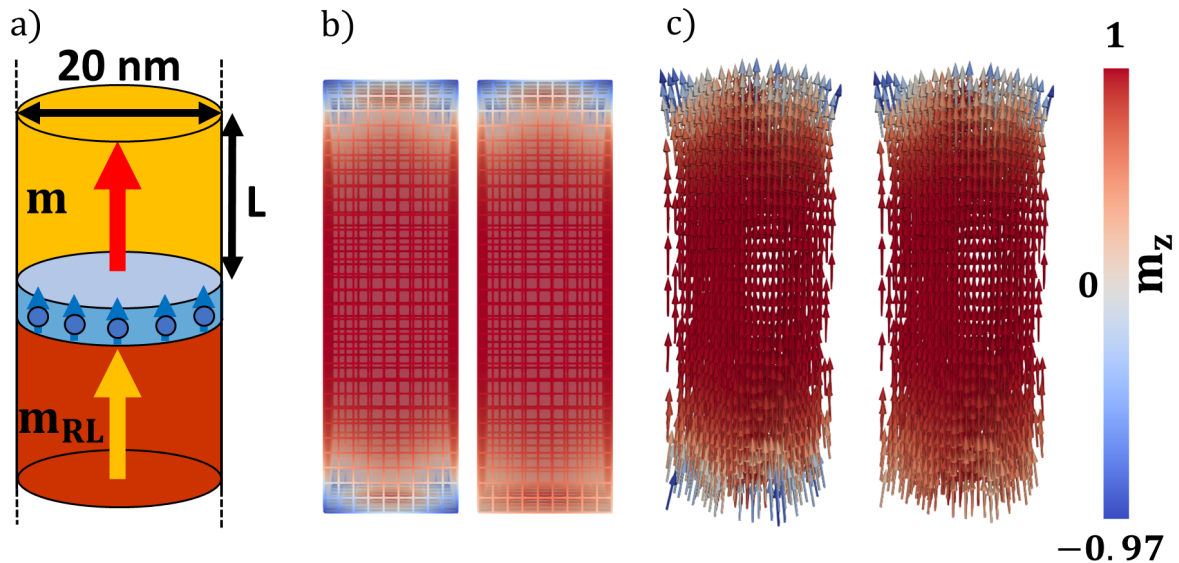


Figure 14: a) Schematic representation of the studied FeCoB pillars with a thickness L and diameter of 20 nm. The effect of the iPMA is represented with blue arrows. The free layer is shown with a yellowish color, the tunnel barrier with a blue color and the reference layer with a reddish color. b) Equilibrium initial state of a thick layer of FeCoB (60 nm) without (left side) and with (right side) iPMA originated by the FeCoB/MgO interface. c) Representation of each elementary cell magnetization resorting to arrows. The color bar indicates the normalized magnitude of the magnetization along the defined z direction (along the pillar axis) in each cell.

5.2.1 STT driven magnetization switching

After the equilibrium state is calculated, a spin-polarized current is applied. The effect of this spin-polarized current on the magnetization dynamics should be included in the LLG equation in a micromagnetic approach. For this purpose, we focus on the damping-like torque term of the LLGS equation:

$$\Gamma_{\text{STT}}^{\text{IP}} = -\gamma a_{\parallel} V_{\text{bias}} \mathbf{m} \times (\mathbf{m} \times \mathbf{m}_{\text{RL}}),$$

where a_{\parallel} is the pre-factor of the damping-like torque, V_{Bias} the applied current bias, \mathbf{m} the normalized magnetization of the free layer and \mathbf{m}_{RL} the normalized magnetization of the reference layer. This equation describes the interaction of the spin polarized current with the

magnetization in each elementary cell of our magnetic volume.

Knowing that the polarization of this spin current is of interfacial origin [66–68], we further describe this effect as evanescent throughout our thick magnetic layer. One way of doing so is considering that the value of a_{\parallel} is decreasing spatially:

$$a_{\parallel}(z) = a_{\parallel}(0) \exp\left\{-\frac{z}{\lambda_{\text{STT}}}\right\}, \quad (47)$$

where λ_{STT} is the factor defining the magnitude of the STT decay throughout the thick layer and $a_{\parallel}(0)$ the magnitude felt at the interface. The origin of the z -axis is at the bottom of the free layer. This decay is similar to the one experienced by the iPMA:

$$K_u(z) = K_u(0) \exp\left\{-\frac{z}{\lambda_{\text{iPMA}}}\right\}, \quad (48)$$

where λ_{iPMA} is the factor defining the magnitude of the decay throughout the thick layer, with $K_u(0) = 0.77 \times 10^6 \text{ J/m}^3$ [69]. Furthermore, both λ_{STT} and λ_{iPMA} equal the length of the elementary cell, implementing a realistic interfacial effect compared with other size values, as shown in figure 15 a). Moreover, the definition of a_{\parallel} must be extended to this

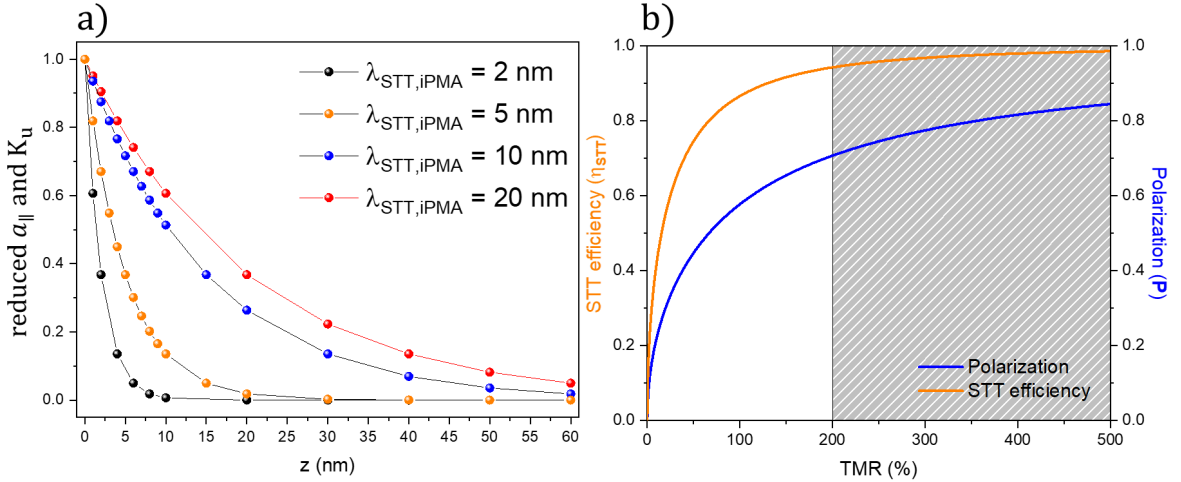


Figure 15: a) Dependency of the defined decay length (20 nm displayed with red spheres, 10 nm with blue spheres, 5 nm with yellow spheres and 2 nm with black spheres) for a normalized value of a_{\parallel} and K_u as a function of the pillar length. b) Polarization (P) and STT efficiency (η_{STT}) as a function of the TMR of the device.

micromagnetic representation. As the field-like torque is neglected in these simulations, a_{\parallel} will influence the voltage necessary for switching. This term was presented before (please refer to equation (15)) as

$$a_{\parallel} = \frac{\hbar}{2e} \frac{\eta_{\text{STT}}}{\text{RA}} \frac{1}{M_s t_{\text{FM}}}.$$

Even though some of its components are constants (\hbar , e and M_s), some of them can be controlled. Examples are the STT efficiency η_{STT} , the RA product and the ferromagnetic length (t_{FM}). The latter must be modified knowing that the STT effect is not affecting

all of the ferromagnetic body, as it would be the case in a macrospin approximation. For this purpose, we consider $t_{\text{FM}} = 2$ nm, as a result of equation (47), knowing that the STT has its full magnitude in the first cell layer. In addition, operable PSA-STT-MRAM pillars can be obtained with a RA product of $2 \Omega \cdot \mu\text{m}^2$. The last quantity to be defined is the STT efficiency η_{STT} . Even though this term is quite complex, it is often considered to be a function of the injected current polarization (P). In the case of an inelastic tunnelling in a symmetric junction, the polarization of the first electrode P_1 is equal to the polarisation of the second electrode P_2 . Thus, $P = P_1 = P_2$, being expressed as [70–72]

$$\eta_{\text{STT}} = \frac{2P}{1 + P^2}. \quad (49)$$

In addition, the polarization in a symmetric junction is related to the TMR as [20],

$$\text{TMR} = \frac{2P^2}{1 - P^2}, \quad (50)$$

leading to

$$P = \sqrt{\frac{\text{TMR}}{\text{TMR} + 2}}. \quad (51)$$

Taking equations (50) and (51) into consideration, one can express η_{STT} as a function of TMR, as shown in figure 15 b). Knowing that, for a working device, our TMR should be higher than 200%, a value of $\eta_{\text{STT}} = 0.94$ was chosen for the simulations. With all these results, one finally obtains a value for $a_{\parallel} = 0.08$ T/V. The different parameters used for the upcoming simulations are presented in table 1. Moreover, the current pulse is described as

Table 1: Material parameters used in the simulations.

M_s (A/m) [20]	A_{ex} (J/m) [20]	K_u (J/m ³) [69]	a_{\parallel} (T/V)
1×10^6	1.5×10^{-11}	0.77×10^6	0.08

a constant pulse of 100 ns with a rising and decay time of 3 ns. This study is then realised on pillars of different thickness, with different applied voltages. From these simulations we expect to extract the mechanism of reversal and the dependency of the switching time on the applied voltage. The last relationship will allow us to infer the switching regime present.

As a first approach, the temporal dependency of the average of the magnetization $\langle m_z \rangle$ at different V_{Bias} is obtained for a pillar with a thickness of 60 nm and lateral size of 20 nm at a temperature of 0 K. In this situation the iPMA is neglected, leading to the obtained data shown in figure 16 a). It is possible to observe that the results are not straightforward with a monotonous behaviour. This can be further analysed when considering 3D snapshots of the magnetization configuration for different time periods for distinct V_{Bias} . In figure 16 b) and 16 c) this is observed for, respectively, -1 V and -1.1 V, represented in figure 16 a) with a red and black color. For both these cases, the nucleation of a domain wall takes place. Afterwards, a different mechanism of reversal occurs. For -1 V, after nucleation, a vortex-like behaviour switches the entire magnetic volume. For the case of -1.1 V, even though there is

a strange behaviour in the beginning, a domain wall is formed, propagating along the thick layer and, eventually, switching the remaining magnetic moments near the top-surface.

This non-uniform behaviour for such close V_{Bias} is associated to the high dependence on the first layer cells magnetization arrangement. Thus, inducing a sturdier perpendicular alignment will alleviate this effect. Moreover, as in a real device we have an underneath MgO tunnel barrier, such sturdier alignment is secured by the induced iPMA. The effect of this additional anisotropy is shown in the time dependency of $\langle m_z \rangle$ for different pillar thickness (30, 40, 50 and 60 nm) for different V_{Bias} , as displayed in figure 17, from which direct conclusions can be obtained.

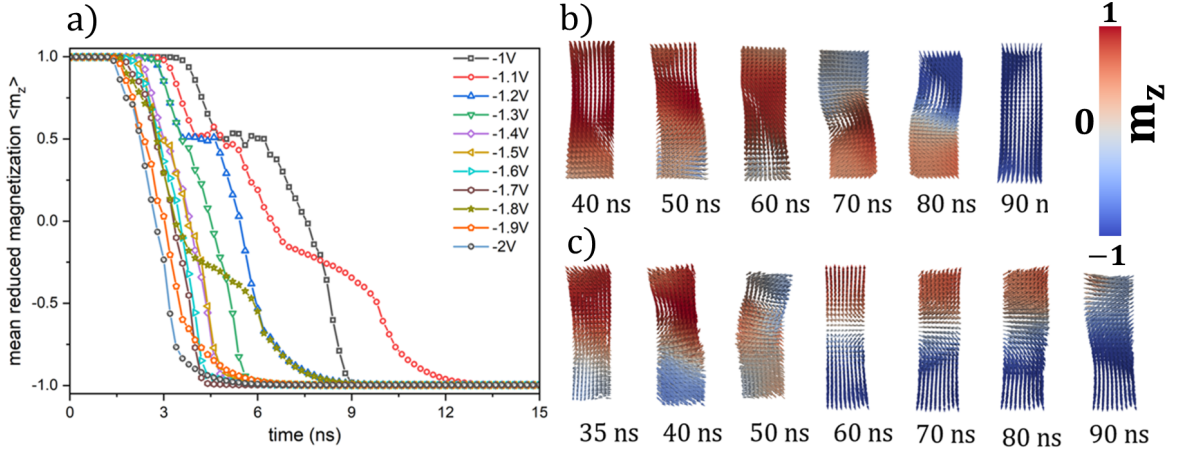


Figure 16: a) Time dependency of $\langle m_z \rangle$ for a pillar thickness of 60 nm with square surface of 20 nm width. Results for different applied V_{Bias} (-1 V to -2 V) at $T = 0$ K. Frames of the magnetization dynamics during the reversal at V_{Bias} of a) -1 V and b) -1.1 V, at different time steps. Snapshots extracted using the Paraview Software.

When comparing the time needed to switch the entire 60 nm magnetic layer, it is observed that the pillar with K_u needs longer time to reverse its magnetization. As the switching is driven by spin transfer torque, and the magnetic moments near the bottom surface are less tilted, longer time will be needed for the effect to be enough to start reversing the first layer of cells. In addition, upon introduction of the additional iPMA, the energy barrier one must overcome to switch the magnetization in the layer is considerably increased. Thus, higher current densities, or similarly, higher V_{Bias} must be applied to switch the magnetic layer.

Further comparisons can be made by individually analysing the different pillar thicknesses. It is observed that the switching mechanism for a thick layer of 30 nm (figure 17, top left panel) and 40 nm ((figure 17, top right panel)) resembles a macrospin-like behaviour, with a sharp variation of the magnetization in a short time interval. This behaviour is different from the one observed for 50 nm (figure 17, bottom left panel) and, principally, 60 nm (figure 17, bottom right panel). In those cases, we observe a shoulder during the magnetization switching, related to a domain wall propagation. A similar behaviour is obtained for the different thickness in the final decay of $\langle m_z \rangle$ (t), regarding the switching of the last layer of cells.

From these data points, it is possible to extract an important feature of the STT-driven switching - the dependency of the switching time (τ_{switch}) with the applied V_{Bias} . This switching time, for a macrospin regime, defines the time the magnetization needs to be perpendicular to the z-axis. However, in micromagnetics, this usually defines the time needed to switch half of the free layer ($\tau_{50\%}$), creating two big magnetic domains, with opposing total magnetization, leading to $\langle m_z \rangle = 0$. However, as in some cases we have a domain wall propagation, we consider the time it takes for 90% of the magnetization to switch ($\tau_{90\%}$), preventing cases where the domain wall would switch back the already switched cell layers. Other important quantity is the nucleation time. In this study, this is defined as the time it takes for the first cell layers to switch ($\tau_{\text{nucleation}}$). In the next studies regarding the switching time behaviour, the $\tau_{90\%}$ value is used. In conventional p-STT-MRAM two different regimes

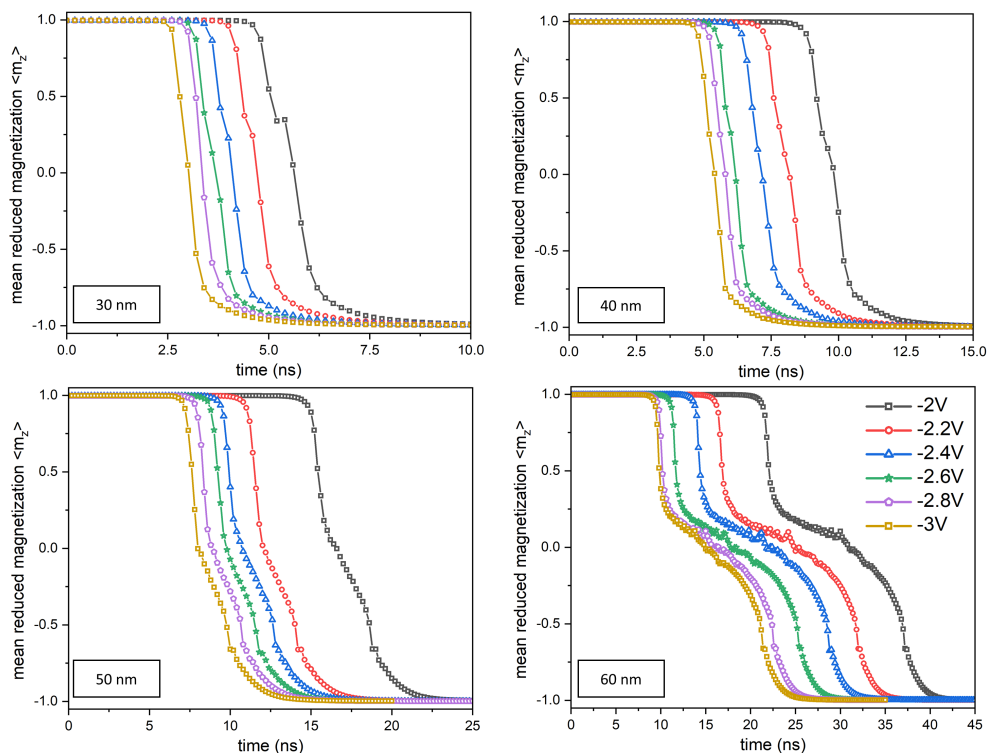


Figure 17: Time representation of the dependency of $\langle m_z \rangle$ for different pillar thickness (30, 40, 50 and 60 nm) for different applied V_{Bias} .

dictate the behaviour of the switching time. In the framework of a macrospin approach, once thermal fluctuations are taken into account, two different regimes are defined: a precessional (ballistic) regime, and a thermally activated regime. One can cross from one to another by varying the amplitude and duration of the supplied current, as observed in figure 18 a). In the first regime, the amplitude of the current supplied is higher than I_{c0} , so the switching time is dependent on the profile of the magnetization. It is possible to define the density of current in this regime as [18, 73]

$$J_c = J_{c0} \left(1 + \frac{\Gamma}{\tau_p} \ln \frac{\pi}{2\theta_0} \right), \quad (52)$$

with θ_0 being an initial angle of misalignment, τ_p the pulse width, Γ a characteristic relaxation time: $\Gamma = (\alpha\gamma\mu_0 H_\perp)^{-1}$, where H_\perp is the existing perpendicular anisotropy fields.

However, as the temperature is added to the system, this relation is no longer valid. First, the initial angle of misalignment θ_0 will follow a Boltzmann distribution, due to the nature of the thermal fluctuations. This will, in addition, create a distribution of the switching currents for a certain pulse width. Moreover, at some point (typical between $\tau_p \approx 50 - 100$ ns), the STT increases the thermal fluctuations in the system, overcoming the energy barrier. This phenomenon can be translated into a thermal activation model

$$J_c = J_{c0} \left(1 - \left(\frac{1}{\Delta} \ln \frac{\tau_p}{\tau_0} \right)^{\frac{1}{2}} \right), \quad (53)$$

where τ_0 is an attempt time, in order of 1 ns [18, 74].

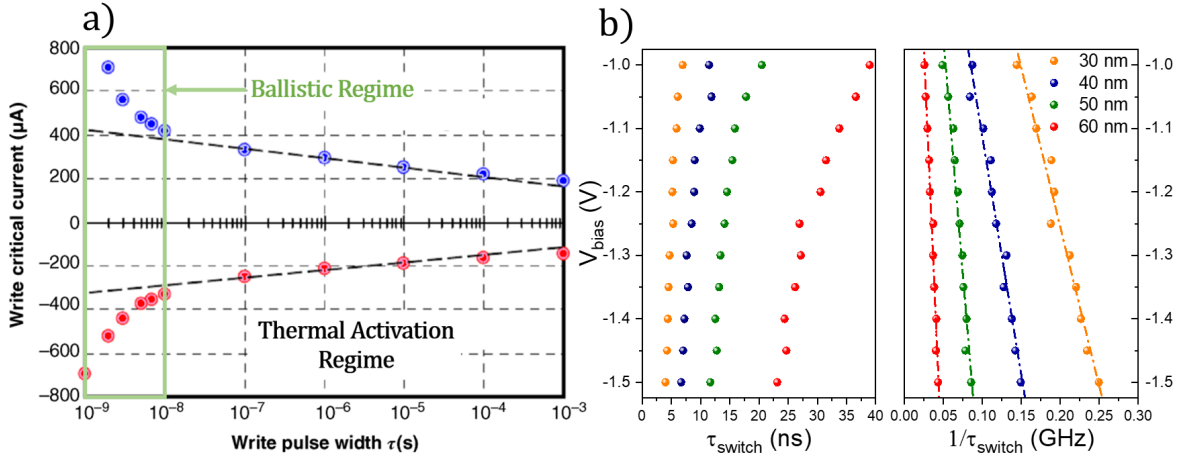


Figure 18: a) Values of STT switching current for different writing pulse widths. A ballistic and a thermal activation regime can be separated. Modified from [20]. b) Dependency of the applied V_{Bias} on (left panel) the switching time and (right panel) the inverse of the switching time. This shows a linear dependency $V_{\text{bias}} \propto \tau_{\text{switch}}^{-1}$. The different lengths are characterized with spheres of different colors. 30 nm is shown with a yellow color, 40 nm with a blue color, 50 nm with green and 60 nm with red.

As the micromagnetic simulations are done neglecting thermal fluctuations, we are directly led to a regime analogous to the ballistic regime, even though the current pulse is of 100 ns. Thus, it is possible to analyse our results regarding the dependency of $\tau_{90\%}$ on the applied V_{Bias} , as shown in figure 18 b). In this regime, we proceed in linearising these data points [75, 76], leading to the dependencies plotted in figure 18 b), right panel. As observed, a linear relationship is observed for an evolution of the applied V_{Bias} with $\tau_{\text{switch}}^{-1}$. This linearity represents a conservation of angular momentum during the switching process [76–78].

Moreover, as the starting point is the same for the different simulations (within the same thickness), the slope associated with this dependency is related with the magnitude of the perpendicular anisotropy field. For PSA this is dominated by the shape anisotropy. Thus, by increasing the thickness, as the effect of the shape anisotropy grows stronger, this slope

will be steeper, as observed.

Even though this data shows a good accordance with theoretically and experimentally obtained results [75, 76, 78], it should be remarked that this linearisation is applicable for a macrospin model. Thus, this result is viewed as an approximation, as the study of these nanoelements can not be done resorting to this model [79]. Moreover, more points are necessary, mainly for lower $|V_{\text{Bias}}|$, for a better fit to this tendency. Furthermore, as we are at 0 K, it is necessary to understand how the magnetization is evolving in time since, in analogy to the ballistic regime, the configuration of the magnetization will dictate the reversal process. For this purpose, from this point onwards, a focus on a single intermediary voltage, $V_{\text{Bias}} = -2.5$ V, is made, thus allowing a comparative study for the different pillar thicknesses, as observed in figure 19 a).

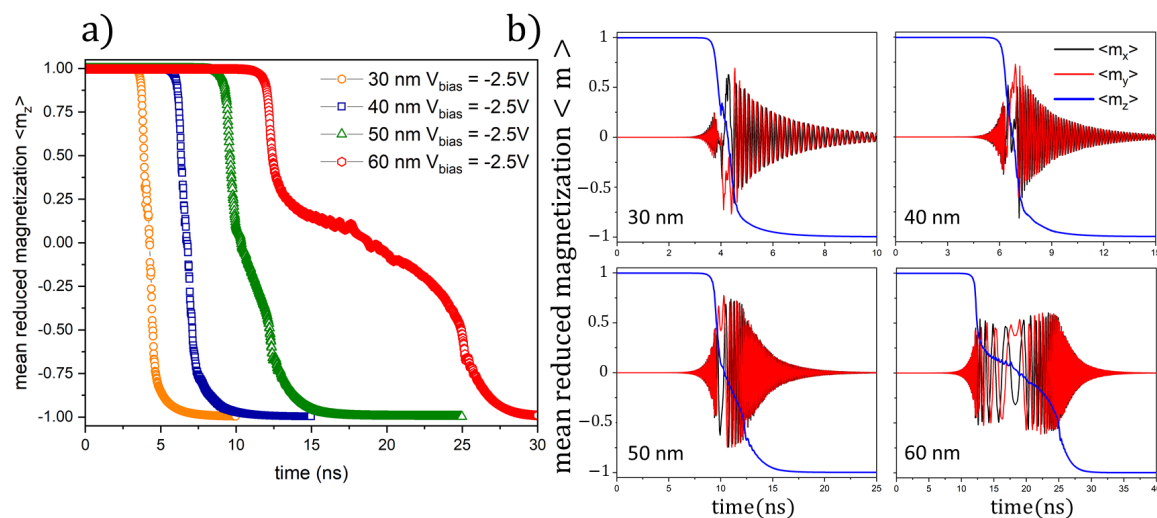


Figure 19: a) Temporal dependency of the mean reduced magnetization $\langle m_z \rangle$ for different pillar thicknesses: 30 nm depicted with orange circles, 40 nm with blue squares, 50 nm with triangles and 60 nm with red circles. b) Temporal dependency of the different components of the magnetization. The mean reduced $\langle m_x \rangle$ is present with a black line, $\langle m_y \rangle$ with a red line and $\langle m_z \rangle$ with a blue line. Results obtained for a V_{Bias} of -2.5 V.

In figure 19 b) it is possible to observe an oscillatory behaviour of the planar mean reduced components of the magnetization $\langle m_{x,y} \rangle$ during reversal. For smaller thickness (30 and 40 nm), the oscillations before half-switch of the magnetic volume have peaks lower than the one right after. For larger thicknesses (50 and 60 nm), these have a similar or the same magnitude, as the reversal mechanism becomes sturdier. In addition, for these thicknesses, there is a time step where a reversal of the planar procession occurs. For a 60 nm thick pillar, this switch is preceded by a decrease in the oscillation frequency and, afterwards, by its sudden increase. For 50 nm, this is not so noticeable as $\langle m_z \rangle$ has a higher decay. Using the different magnetization components it is possible to trace the associated switching diagram for each layer thickness at $V_{\text{Bias}} = -2.5$ V, represented in figure 20. From these trajectories an additional confirmation, that the underlying mechanism in these structures is not macrospin, can be inferred. Even though for 30 and 40 nm this is not immediately clear, the total

magnitude of the magnetization vector, for each data point, $\langle m \rangle^2 = \langle m_x \rangle^2 + \langle m_y \rangle^2 + \langle m_z \rangle^2$ is not unitary. This is in resemblance with a micromagnetic understanding and is more noticeable for 50 and 60 nm, where the switching does not follow the unitary sphere. Moving

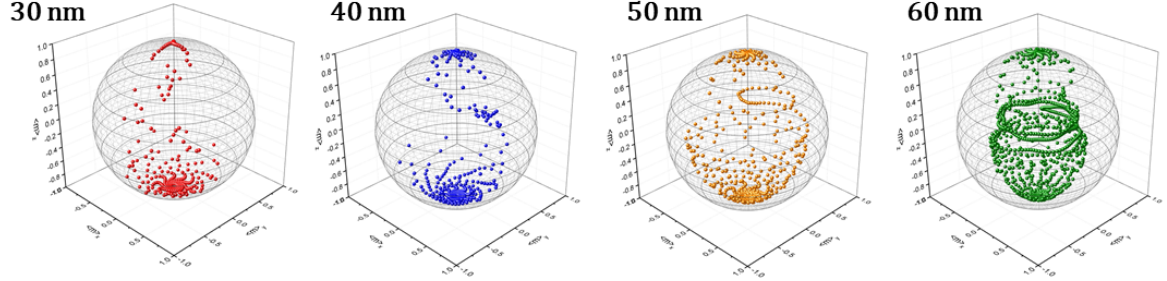


Figure 20: Switching trajectory for a thick layer of 30 nm (red points), 40 nm (blue points), 50 nm (golden points) and 60 nm (green points). The z axis represents $\langle m_z \rangle$ and the basal plane (x and y axis) represents $\langle m_{x,y} \rangle$. The simulated data is contained in a macrospin sphere (radius 1). Results obtained for V_{bias} of -2.5 V.

forward a study on the 3D magnetization profile at different time steps for each thickness is made. As we are at 0 K, this configuration will dominate the switching time. For this purpose, different snapshots are presented in the next figures for different pillar thickness. In all of them, the first and last steps of the integration interval are present, and the events of $\tau_{\text{nucleation}}$, $\tau_{50\%}$ and $\tau_{90\%}$ shown at bold. As usual, the color plot displays the magnitude of the normalized magnetization along z, figure 21. Starting with lower thicknesses, as expected, there is no resemblance with a macrospin picture. However, there is no clear mechanism associated with the reversal process, as the full magnetic layer is interacting and switching in a collective curling-like behaviour. This can be further seen when considering the magnetization profile at $\tau_{50\%}$. There is the formation of two big head-to-head magnetic domains, however, the switched domain is placed near the top surface, while the STT is being pumped at the bottom surface. Moreover, two different frames, at 4.2 and 4.3 ns, confirm that this switching is not propagating along the symmetry axis. This behaviour is further observed for a thickness of 40 nm. For 50 and 60 nm, the nucleation of a domain wall starts in the bottom surface, further creating a domain wall near the middle of the pillar. For the frame $\tau_{50\%}$, two magnetic domains can be observed, in a configuration tail-to-tail. Additionally, the domain wall has magnetic moments in a perpendicular placement, compared with the main domains. This domain wall subsequently propagates along the symmetry axis of the magnetic layer, while it rotates in the basal plane. This mechanism of reversal is identifiable as a tail-to-tail Transverse Domain Wall (TDW) [80–83].

As it was observed that there is a modification in the reversal mechanism by varying the layer thickness, intermediate values were taken between 40 and 60 nm, analysing the evolution of the collective curling-like reversal state to the sturdy TDW. In figure 22 the temporal dependency of $\langle m_z \rangle$ for a single voltage of -2.5 V is observed for a variation of

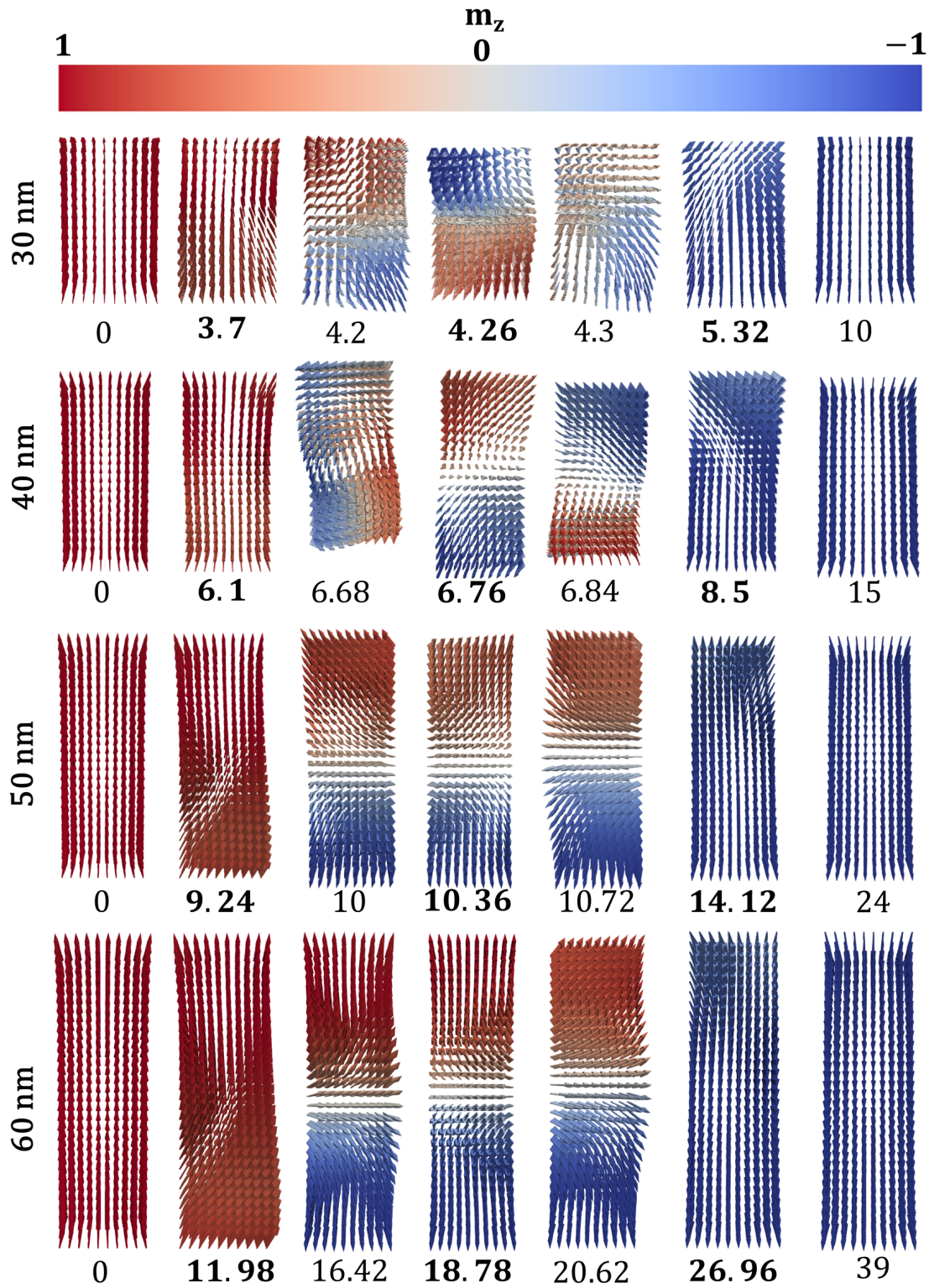


Figure 21: Snapshots at different time steps for a 30, 40, 50 and 60 nm thick magnetic layer, for an applied voltage of -2.5 V. The $\tau_{\text{nucleation}}$, $\tau_{50\%}$ and $\tau_{90\%}$ are shown at bold. The color is representative of the magnitude of \mathbf{m}_z and quantified in the color plot. It is observed a collective curling-like reversal for thicknesses of 30 and 40 nm. For 50 and 60 nm the reversal mechanism is based on a transverse domain wall nucleation and propagation.

the magnetic layer thickness. After a threshold thickness value of 48 nm, the appearance of a slower $\langle m_z \rangle$ decay state appears, associated with the propagation of a TDW. This is more pronounced for thicker layers, as the domain wall has to travel larger distances and, as the effect of the shape anisotropy is stronger, for the same applied voltage, the domain wall motion will take longer time. A comprehensive study can be performed taking into consideration the maximum value of the mean energies of the magnetic system as a function of the layer thickness (see figure 23). Analysing figure 23 a), two regimes can be seen, dividing

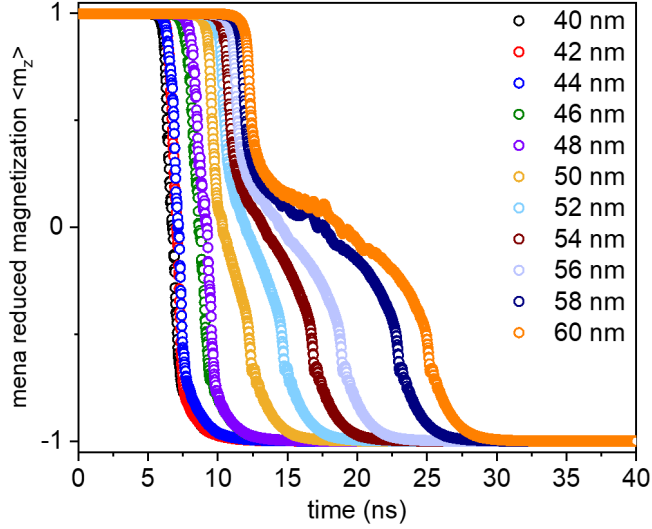


Figure 22: Evolution of the Domain Wall Motion behaviour for thickness of 40 nm to 60 nm with an applied voltage of -2.5 V. The mean reduced magnetization $\langle m_z \rangle$ is displayed for each pillar thickness.

the reversal mode as a collective curling-like reversal and transverse domain wall switching. For further comparison, the quantities represented are minimized by the higher total density of energy, obtained for a pillar thickness of 42 nm. The three different energy contributions are then considered, E_{exchange} , E_{Ku} and E_{shape} . The uniaxial contribution remains fairly constant through the increase in the layer thickness, as its effect is pronounced during the nucleation process, near the bottom-surface of the pillar. The other two contributions show a transition behaviour after the 48 nm pillar threshold, associated with a transformation from the collective curling-like switching state to the domain wall-based switching. Starting with E_{exchange} , below the 48 nm threshold, as observed in the frames of figure 21 for a thickness of 30 and 40 nm, both bottom and top surface magnetization cells are switching simultaneously, typical of a curling-like reversal. This will result in a high E_{exchange} . In contrast, when forming a domain wall, there is a minimization of this energy, as the interaction between neighbouring magnetic moments is smoother throughout the thick magnetic layer. The same transition can be observed for E_{shape} as, when creating the domain wall, the transverse component of the magnetization will increase this energy term. Both these interactions lead to a decrease in total energy of the magnetic system.

Furthermore, it is interesting to investigate the dependency of the different proposed processes time, such as $\tau_{\text{nucleation}}$, $\tau_{50\%}$ and $\tau_{90\%}$, depicted in figure 23 b), as a function of the pillar thickness. Below the threshold thickness, there is no clear trend present. This is a viable conclusion as, for this range of thickness, the switching mechanism is not well defined. After the transition region, these three quantities follow a linear dependency with increasing thickness where the lowest variation is obtained for the nucleation time and the highest for the $\tau_{90\%}$ process.

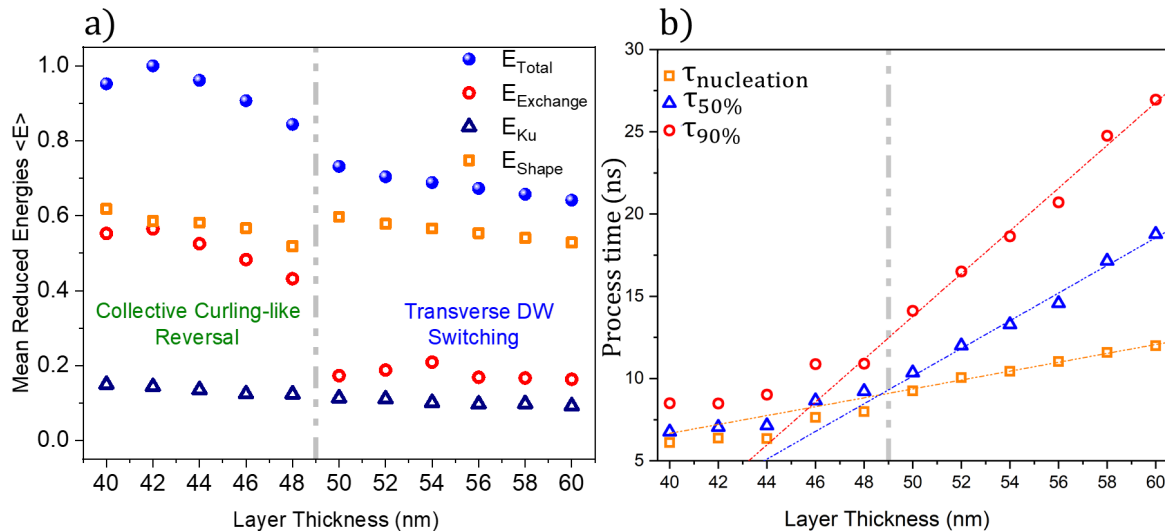


Figure 23: Dependence of the a) mean reduced energies of the magnetic system, normalized by the maximum value of the total energy (E_{total} shown with blue spheres, E_{exchange} with red circles, E_{Ku} with blue triangles and E_{shape} with orange squares) and b) the process time ($\tau_{\text{nucleation}}$ shown with orange squares, $\tau_{50\%}$ with blue triangles and, with red circles, $\tau_{90\%}$ as a function of the pillar thickness for an applied voltage of -2.5 V.

As stated before, this study is being made using a squared shaped pillar. This representation is not realistic regarding the final patterned device and, consequently, holds an approximate image of the expected behaviour of the PSA-STT cell. Nevertheless, the emphasis of the study is not on a quantitative comparison with experimental data, but on understanding the dynamical behaviour of the magnetization reversal. Hence, understanding how this intrinsic mechanism would behave for a different mesh size and shape is relevant. For this purpose, a study on a squared pillar with 1 nm mesh and circular like pillar with 1 nm and 2 nm mesh size is realised. The latter, as explained before, is based on a staircase-like shape. In figure 24 a) the shape of this distinct meshes is shown and, in figure 24 b) the temporal dependency of the mean reduced magnetization is shown. As a first approach, we can compare the outcome of a mesh of 2 nm in both a squared and circular like surface. This effect is quite clear. Even though the dynamical behaviour is conceptually the same, there is an increase in the different process times, nominatively in $\tau_{50\%}$ and $\tau_{90\%}$. We further extend this study to a 1 nm mesh size. However, for this mesh size, the computation time is significantly higher, as the time step is reduced for convergence. Moreover, a higher voltage is needed for the switching to take place, as we are extracting data points where the magnetization was not entirely parallel

to the polarisation of the electrons. In addition, as we are varying the cell size by half, the value of a_{\parallel} will double. Thus, in order to get faster results, a voltage of -3.5 V was used. From the obtained results we can infer that the reversal mechanism remains the same, even though there are some differences in the time that the domain wall takes to propagate. This difference is analogous to the case of the 2 nm mesh and can be understood as an artefact derived from the extraction of the edge cells. As this study is made at 0 K the behaviour of the magnetization is highly dependable of the misalignment of the initial cell layers. This problem can be resolved by adding an initial small misalignment of the magnetization in the cells of the magnetic volume [69]. Nonetheless, comparisons made with experiments would

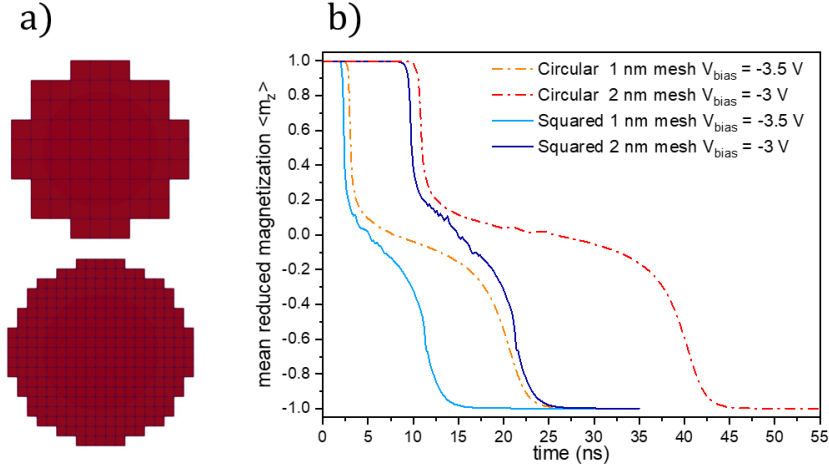


Figure 24: a) Effect of the mesh grid on the reversal mechanism of a squared (2 nm mesh with a blue color and 1 nm mesh with light blue) and circular (2 nm mesh with a red color and 1 nm with orange color) shaped pillar. For all cases the used value of a_{\parallel} is of 0.08 T/V. b) Shape of the pillar surface for 2 nm mesh and 1 nm mesh circular based pillar.

resort to some temperature range, where the thermal fluctuations would induce a random initial angle of misalignment. Thus, the possibility of further reducing the mesh size for room temperature simulations opens the possibility of higher accuracy in our simulations.

From this subsection one can conclude that the reversal mechanism is based on a transverse domain wall nucleation and propagation for thicker layers (50 nm and 60 nm) and a collective curling-like switching state for thinner layers (30 nm and 40 nm). The switching for all these free layer thicknesses is present in a regime analogous to the ballistic regime, as it follows a linear dependency on $V_{\text{Bias}} \propto \tau_{\text{switch}}^{-1}$. However, these results are obtained for a simulation at 0 K which is, experimentally, impossible, for the final purpose of these devices. Thus, one should analyse how the switching mechanism reacts to the influence of thermal fluctuations.

5.2.2 Temperature study

The study of thermal effects in our system can be made by analysing the motion of the magnetization in contact with a heat bath of temperature T . This dynamic is correctly described as a Langevin equation in the form of a stochastic relation

$$\frac{d\mathbf{X}}{dt} = \mathbf{a}(\mathbf{X},t) + b(\mathbf{X},T)\eta(t) \quad (54)$$

where \mathbf{X} is the variable under study (magnetization), $\eta(\mathbf{X},t)$ the noise term, $\mathbf{a}(\mathbf{X},t)$ and $b(\mathbf{X},t)$ are, respectively, the drift and diffusion term.

This thermal noise is implemented by taking into consideration the Brown theory, being translated as a random field term, \mathbf{H}_{th} , described as a Gaussian distribution with a mean value given by $\langle \mathbf{H}_{\text{th}}(\mathbf{r}_i, t_k) \rangle = 0$, and an autocorrelation function of

$$\langle \mathbf{H}_{\text{th}}(\mathbf{r}_1, t_1) \cdot \mathbf{H}_{\text{th}}(\mathbf{r}_2, t_2) \rangle = \mathcal{D}\delta(\mathbf{r}_1 - \mathbf{r}_2)\delta(t_1 - t_2), \quad (55)$$

where \mathcal{D} is the variance expressed as [20,22]

$$\mathcal{D} = \frac{2\alpha k_B T}{\mu_0^2 M_s V \gamma}.$$

This thermal field is taken into consideration as an additional term in the effective field equation (please refer to equation (44)). Since this field is random, it takes into account stochastic processes. Therefore, the following simulations are performed several times, obtaining a statistic result.

For a first study, a pillar thickness of 60 nm was selected and a study on the evolution of the magnetization was done at a temperature of 300 K. This dependency is obtained for 100 events and for a range of applied voltages from -2 V to -4 V. In figure 25 a) the temporal evolution of $\langle m_z \rangle$ for an applied voltage of -2 V, -3 V and -4 V is shown for different integration times (15 ns, 12 ns and 10 ns, respectively). It is observed that, for a higher voltage applied, the dispersion in the data points is reduced. It is also obvious that the reversal is starting sooner, as the thermal fluctuations drive the magnetization near the bottom surface away from its equilibrium orientation. Therefore, there is a higher torque experienced by the first-layer cells, which will reduce the nucleation time. The time distribution can be further analysed by considering the statistical dispersion of $\tau_{\text{nucleation}}$, $\tau_{50\%}$ and $\tau_{90\%}$, represented in figure 25 b). The histograms were produced taking into consideration a bin size of 0.25 ns and enveloped by a lognormal distribution curve. For the three different process times, at larger V_{Bias} both the event time and the distribution width become smaller.

As this behaviour is expected for a ballistic regime [84], the mean values for the different distribution curves were extracted in order to confirm this premise, as displayed in figure 26. We further observe that this relation is linear as a function of the inverse switching time ($V_{\text{Bias}} \propto \tau_{\text{switch}}^{-1}$). This demonstrates that, in addition to the mechanism of reversal based on transverse domain wall being robust against thermal fluctuations, the switching reversal

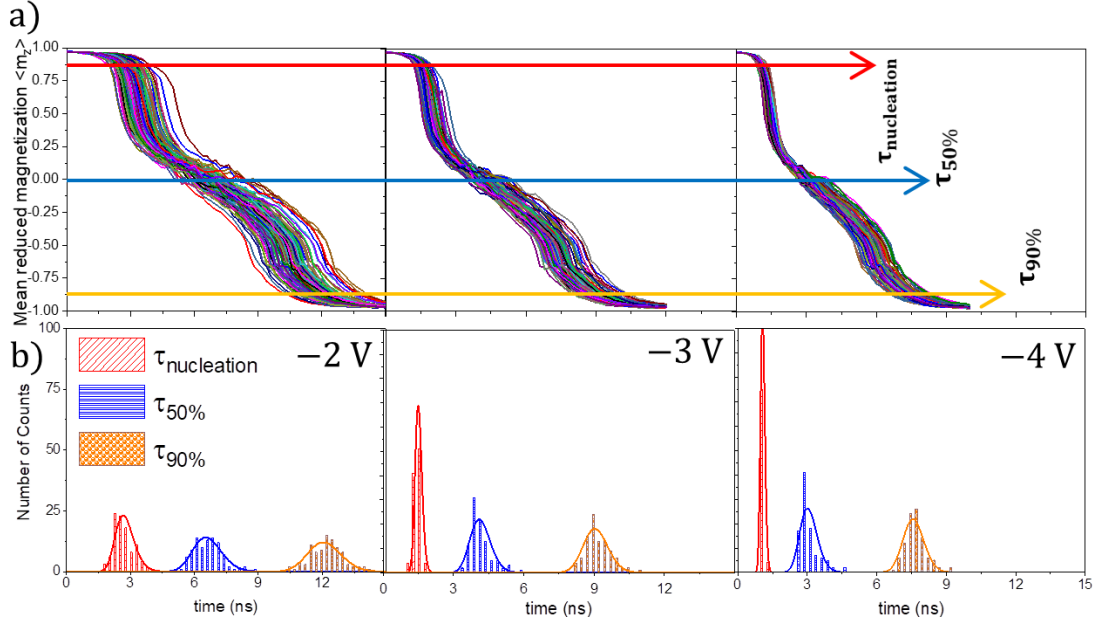


Figure 25: Time evolution of a) 100 events of the mean reduced magnetization $\langle m_z \rangle$ at different applied voltages (from left to right, -2 V, -3 V and -4 V) b) The distribution of the different process, associated with each magnetization curves. The histograms are realised with 0.25 bin size and are enveloped with a lognormal distribution curve. $\tau_{\text{nucleation}}$ is shown with a red colour, $\tau_{50\%}$ with a blue curve and $\tau_{90\%}$ with orange color. Results obtained for a temperature of 300 K and pillar thickness of 60 nm and 20 nm diameter.

happens in the ballistic regime. The slope from this relation is, as for the case of 0 K, different for the different events, as expected from the action of a domain wall nucleation and propagation.

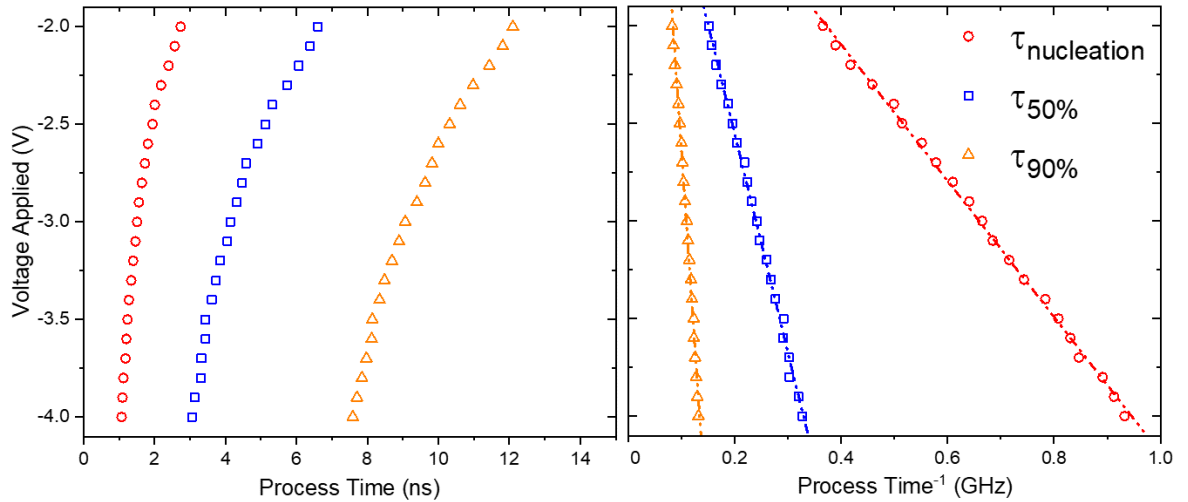


Figure 26: Applied voltage as a function of the process time ($\tau_{\text{nucleation}}$, $\tau_{50\%}$ and $\tau_{90\%}$) and of the inverse of the process time. $\tau_{\text{nucleation}}$ is depicted with a red color, $\tau_{50\%}$ with blue color and $\tau_{90\%}$ with orange color. Results obtained for a pillar thickness of 60 nm and diameter of 20 nm for a temperature of 300K.

It is also interesting to study what is the behaviour of these distributions with an increase in temperature. For this purpose, a temperature ranging from 50K to 350 K analysis is realised. Selected distributions are shown in figure 27.

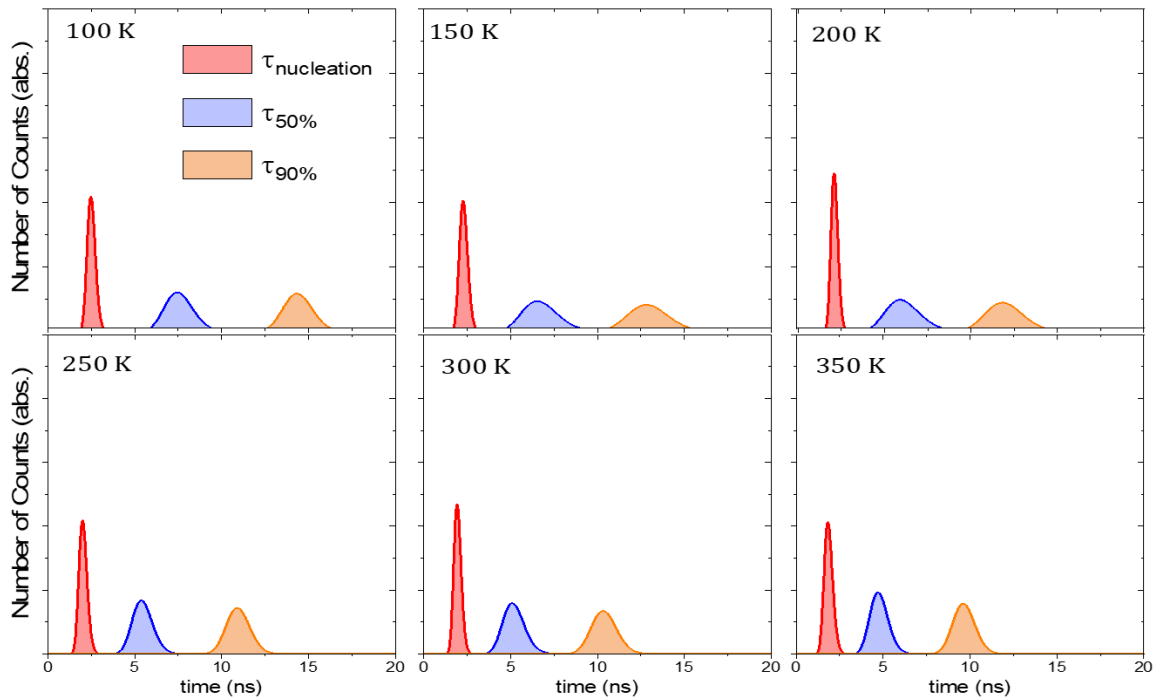


Figure 27: Lognormal distribution for the different processes. With a red color the $\tau_{\text{nucleation}}$ is identified, with blue the $\tau_{50\%}$ and, with orange, $\tau_{90\%}$. Evolution for temperatures ranging 100 K until 350 K (50 K step). Results obtained for a 60 nm thick pillar with diameter of 20 nm for an applied bias of -2.5 V. Bin size of 0.25 ns.

One can observe that, as the temperature rises, $\tau_{50\%}$ and $\tau_{90\%}$ diminish. This does not hold true for $\tau_{\text{nucleation}}$. This is a consequence of the ballistic regime as, with some thermal fluctuations, the switching will happen faster but is not dependent on the temperature, as the STT dominates the switching. This can be further seen in figure 28. From this display, it is observed that the mean switching time quickly reaches a minimum value. This is more sharp for the case of the nucleation, as the thermal fluctuations help to start the nucleation process but, as the STT dominates, do not affect further the switching times. Moreover, taking into consideration these process times for the case of 0 K, a smooth exponential fit is done, observing the important effect of the temperature on the start of the magnetization reversal.

Regarding smaller thicknesses, it is observed that we are still present in a ballistic regime. This is observed in the linear relationship of figure 29. In addition, we are still present in a collective curling-like reversal as the slope of the different events is nearly equal but, still, not the same, as it would be the case of a macrospin-like based switching.

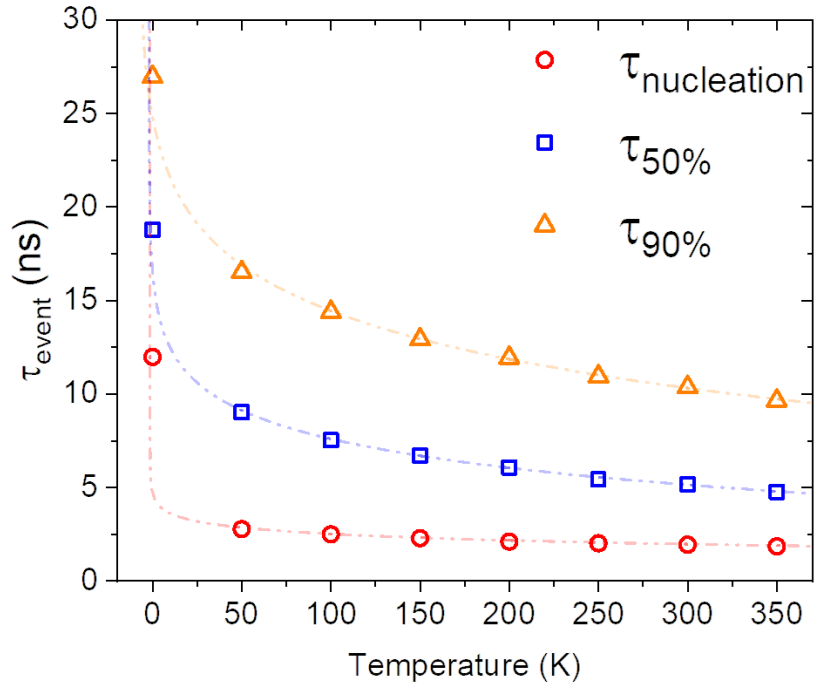


Figure 28: Different process time (ns) for a Temperature evolution (from 0 K to 350 K). With red circles we observe $\tau_{\text{nucleation}}$, blue squares the $\tau_{50\%}$ and orange triangles $\tau_{90\%}$. The data points are fit with an exponential function.

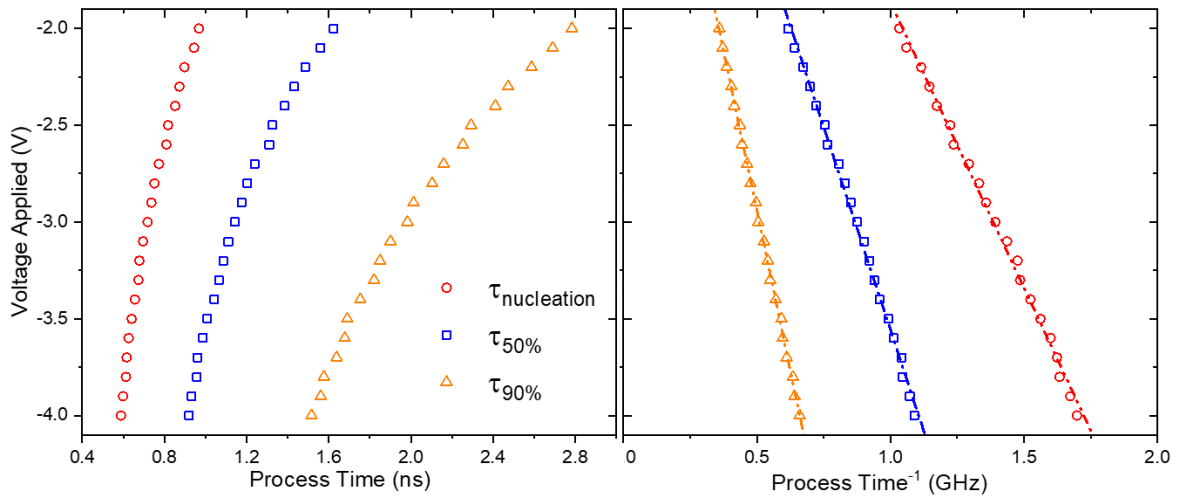


Figure 29: Applied voltage as a function of the process time (ns) and the inverse of the process time. The $\tau_{\text{nucleation}}$ is depicted with a red color, the $\tau_{50\%}$ with blue color and $\tau_{90\%}$ with orange color. Results obtained for a thickness of 30 nm with a diameter of 20 nm for a temperature of 300K.

6 Conclusions

The Perpendicular Shape Anisotropy Spin Transfer Torque Magnetic Random Access Memory (PSA-STT-MRAM) shows promising results in obtaining high thermal stability values at technology nodes below 20 nm. However, being an emerging technology, it still faces nanofabrication challenges, such as the possibility of tilted pillars.

In the present dissertation a methodology has been proposed to determine the possible tilt angle of the PSA-STT-MRAM pillars, which may result during the patterning process due to the etching of pillars to high aspect ratios. The procedure involves measurements of the coercivity of the storage layer for various directions of the applied magnetic field, within two orthogonal planes, implemented by Nicolas Perrissin and Gabin Grégoire. The interpretation of these results was based on the 3D Stoner-Wohlfarth model. The studied pillar was fabricated in the *Plateforme de Technologie Amount* (PTA) in Grenoble, by the MRAM group. Qualitatively, for the used storage layer geometry (13 nm in diameter, 60 nm in thickness), the magnetization reversal was found to occur via domain wall nucleation/propagation when the field is applied along the easy axis, and via coherent rotation, when it lies in the hard plane. Moreover, similar results would be obtained regarding an easy-cone state in a conventional STT-MRAM, as the easy axis of the magnetization is misaligned relative to the perpendicular axis. Therefore, this study might be also useful for this regime, as one can measure the desired hysteresis loops and calculate the cone angle simultaneously.

Through the use of a micromagnetic solver written by Liliana Buda Prejbeanu, a researcher at Spintec, it was possible to identify different aspects of the magnetization reversal in the PSA-STT-MRAM. This study comprised pillars of different height (30, 40, 50 and 60 nm), with a diameter of 20 nm. A broad range of applied voltages were considered. Further simulations implementing thermal fluctuations were performed. It was shown that, below a threshold thickness of 50 nm, the mechanism of reversal resembles a collective curling-like reversal. Above this threshold, a transverse domain wall is nucleated at the bottom surface, propagating along the symmetry axis of the pillar. A slowing down of the reversal dynamics is observed in the transverse domain wall regime when the domain wall is located around mid-thickness of the storage layer. That effect increases as the layer grows thicker. It was examined that the reversal mechanism remains the same for different mesh dimensions. It was further observed that the inverse of the switching time follows a linear relation with the applied bias voltage. For the different thicknesses, the slope of $V_{\text{bias}}(\tau_{\text{switch}}^{-1})$ grows steeper as the thickness increases, due to a reinforcement of the perpendicular shape anisotropy in the storage layer. Moreover, the $V_{\text{bias}}(\tau_{\text{switch}}^{-1})$ dependence remains linear, when considering thermal fluctuations. This demonstrates that, even though the nucleation process is assisted by thermal fluctuations, the switching is controlled by the STT. Thus, it is important to understand the physical phenomena behind the magnetization reversal driven by STT for further development of optimized devices. In addition, it was observed that the reversal mechanism is robust against thermal fluctuations. This work is assisting the understanding of the real-time switching behaviour in the PSA-STT-MRAM memory cells, currently being

under study at SPINTEC (Grenoble).

As my future PhD work at SPINTEC, the etching step during the nanofabrication will be modified in order to reduce the pillar aspect-ratio. This will be done by filling a semiconductor vertical interconnect (via) with the thick magnetic free layer using electrochemical deposition. Afterwards, the remaining stack is deposited on top of the via and electrically connected through subsequent lithography steps. As the diameter of the interconnects can be controlled, a reduced variability in the dimensions of the resulting devices is expected. In addition, there are no tilted or fallen pillars, improving the reproducibility. It is expected that this approach will lead to a fully functional memory, paving the way towards the integration of the PSA-STT-MRAM in a viable technological process, compatible with a high areal density and mass production.

References

- [1] Steven Lohr, 'Big Data's Impact in the World', 2012. Retrieved from: <https://www.nytimes.com/2012/02/12/sunday-review/big-datas-impact-in-the-world.html>
- [2] John Loeffler, 'No more transistors: the end of moore's law', 2018. Retrieved from: <https://interestingengineering.com/no-more-transistors-the-end-of-moores-law>
- [3] Yole Developpment, "Emerging Non-Volatile Memory", 2017. Retrieved from: https://pt.slideshare.net/Yole_Developpement/emerging-nonvolatile-memory-2017-report-by-yole-developpement
- [4] C. Associates, "Emerging Memories Ramp Up Report," *Goughlin Associates and Objective Analysis*, Tech. Rep., 2019
- [5] Semiconductor Engineering, 'Next-gen memory ramping up', 2018. Retrieved from: <https://semiengineering.com/next-gen-memory-ramping-up/>
- [6] Lam Research, "Tech brief: Much ado about memory", 2018. Retrieved from: <https://blog.lamresearch.com/tech-brief-much-ado-about-memory/>
- [7] Lam Research, "Tech brief: ABCs of new memory," 2018. Retrieved from: <https://blog.lamresearch.com/tech-brief-abcs-of-new-memory/>
- [8] CYPRESS, "Memories for Embedded Systems - NVSRAM", *n.d.*. Retrieved from: <https://www.cypress.com/products/nvsram-nonvolatile-sram>
- [9] CYPRESS, "F-ram (Non Volatile Ferroelectric Ram)," *n.d.*. Retrieved from: <https://www.cypress.com/products/f-ram-nonvolatile-ferroelectric-ram>
- [10] M. Trentzsch, S. Flachowsky, R. Richter *et al.*, "A 28 nm HKMG super low power embedded NVM technology based on ferroelectric FETS," *IEDM*, San Francisco, CA, 2016, pp. 11.5.1-11.5.4
- [11] N. Xu, B. Gao, L. F. Liu *et al.*, "A unified physical model of switching behaviour in oxide-based RRAM," *2008 Symposium on VLSI Technology*, Honolulu, HI, 2008, pp. 100-101
- [12] J. Guy, "Evaluation of the performances of scaled CBRAM devices to optimize technological solutions and integration flows," PhD dissertation, University of Grenoble Alpes, 2015
- [13] X. Dong, N. P. Jouppi and Y. Xie "PCRAMsim: system-level performance, energy, and area modelling for Phase-Change Ram," *Proceedings of ICCAD*, San Jose, CA, 2009, pp. 269-275
- [14] i-Micronews, "MRAM: a promising new life after eFlash - an interview with GlobalFoundries," 2019. Retrieved from: <https://www.i-micronews.com/mram-a-promising-new-life-after-eflash/>
- [15] T. Coughlin, "Emerging Memories and Artificial Intelligence", 2019. Retrieved from: <https://www.forbes.com/sites/tomcoughlin/2019/09/09/emerging-memories-and-artificial-intelligence/#296d89e421bb>
- [16] T. Coughlin, "\$20B Emerging Memory Market by 2029", 2019. Retrieved from: <https://www.forbes.com/sites/tomcoughlin/2019/07/09/20b-emerging-memory-market-by-2029/#795e52f922ef>
- [17] I. Žutić, J. Fabian and S. D. Sarma, *Rev. Mod. Phys.* **76**, 323 (2004)
- [18] D. Apalkov, B. Dieny and J.M. Slaughter, *Proceedings of the IEEE* **10**, 1796 (2016)
- [19] S. Ikeda, J. Hayakawa, Y. Ashizawa *et al.*, *App. Phys. Letters* **93**, 082508 (2008)
- [20] B. Dieny, R. B. Goldfarb and K. Lee, *Introduction to Magnetic Random-Access Memory*. Wiley-Blackwell, 2017
- [21] S. Bhatti, R. Sbiaa, A. Hirohata *et al.*, *Materials Today* **20**, 530 (2017)
- [22] W. Brown, *Phys. Rev.* **130**, 1677 (1963)

- [23] N. Locatelli, V. Cross and J. Grollier, *Nat. Mat.* **13**, 1 (2013)
- [24] S. Ikeda, K. Miura, H. Yamamoto *et al.*, *Nat. Mat.* **9**, 721 (2010)
- [25] B. Dieny and A. Vedyayev, *EPL*, **25**, 723 (1994)
- [26] A. A. Timopheev, R. Sousa, M. Chshiev *et al.*, *Sci. Rep.* **6**, 26877 (2016)
- [27] Y. Fu, I. Barsukov, J. Li *et al.*, *App. Phys. Lett.* **108**, 142403 (2016)
- [28] B.M.S Teixeira, A. A. Timopheev, N. Caçoilo *et al.*, *App. Phys. Lett* **112**, 202403 (2018)
- [29] B.M.S Teixeira, A. A. Timopheev, N. Caçoilo *et al.*, *Phys. Rev. B* **100**, 184405 (2019)
- [30] C. Yoshida, T. Tanaka, T. Ataka *et al.*, *Jpn. J. Appl. Phys.* **58**, SB3B05 (2019)
- [31] H. Sato, S. Ikeda and H. Ohno, *Jpn. J. Appl. Phys.* **56**, 0802A6 (2017)
- [32] L. Thomas, G. Jan, J. Zhu *et al.*, *J. App. Phys* **115**, 172615 (2014)
- [33] N. Perrissin, S. Lequeux, N. Strelkov *et al.*, *Nanoscale*, **10**, 12187 (2018)
- [34] K. Watanabe, B. Jinnai, S. Fukami *et al.*, *Nat. Comm.* **9**, 663 (2018)
- [35] N. Perrissin, N. Caçoilo, G. Gregoire *et al.*, *J. Phys. D: App. Phys* **52** 505005
- [36] M. T. Johnson, P. J. H. Bloemaen, F. J. A. Broeder *et al.*, *Rep. Prog. Phys* **59**, 1409 (1996)
- [37] S. Blundell, *Magnetism in Condensed Matter*, Oxford University Press, 2001
- [38] B. Patrick, *Physical origins and theoretical models of magnetic*, 1993. Retrieved from: http://www1.mpi-halle.mpg.de/bruno/publis/R_1993_1.pdf
- [39] D. C. Ralph and M. D. Stiles, *Journ. Magn. Magn. Mat.* **320**, 1190 (2008)
- [40] S. Oh, S. Park, A. Manchon *et al.*, *Nature Phys* **5**, 898 (2009)
- [41] A. A. Timopheev, R. C. Sousa, M. Chshiev *et al.*, *Phys. Rev. B* **92**, 104430 (2015)
- [42] Z. Li, S. Zhang, Z. Diao *et al.*, *Phys. Rev. Lett.* **100**, 246602 (2008)
- [43] H. X. Yang, M. Chshiev, B. Dieny *et al.*, *Phys. Rev. B* **84**, 054401 (2011)
- [44] S. Baumann, F. Donati, S. Stepanow *et al.*, *Phys. Rev. Lett.* **115**, 237202 (2015)
- [45] A. Aharoni, *Introduction to the Theory of Ferromagnetism*, Oxford University Press, 2001
- [46] D. J. Craik and R. S. Tebble, *Rep. Prog. Phys* **24**, 116 (1961)
- [47] J. Slonczewski, *J. Magn. Magn. Mat.* **159**, L1 (1996)
- [48] L. Berger, *Phys. Rev. B* **54**, 9353 (1996)
- [49] Y. Huai, P. Nguyen, F. J. Albert *et al.*, *App. Phys. Lett.* **84**, 3118 (2004)
- [50] A. Aharoni, *Phys. B: Cond. Matt.* **306**, 1 (2001)
- [51] R. Sousa, "Spintronics memory function: materials and device concepts. Mesoscopic systems and quantum hall effect", *Habilitation à diriger der recherches*, University Grenoble Alpes (2017)
- [52] T. Kishi, H. Yoda and T. Kai, "Lower Current and fast switching of a perpendicular (TMR) for high speed and high density spin-transfer-torque MRAM", in *2008 IEEE International Electron Devices Meeting (IEDM)*, San Francisco, CA, 2008, pp. 1-4
- [53] M. Sato, *J. App. Phys.* **66**, 983 (1989)
- [54] S. S. P Parkin and D. Mauri, *Phys. Rev. B* **44**, 7131 (1991)
- [55] M. A. Ruderman and C. Kittel, *Phys. Rev.* **96**, 99 (1954)
- [56] S. Bandiera, R. C. Sousa, Y. Dahmane *et al.*, *IEEE Magn. Lett.* **1**, 3000204 (2010)
- [57] H. Sato, M. Yamanouchi, S. Ikeda *et al.*, *App. Phys. Lett.* **101**, 022414 (2012)
- [58] N. Perrissin, "Miniaturisation extrême de mémoires STT-MRAM: couche de stockage à anisotropie de forme perpendiculaire," PhD dissertation, University of Grenoble Alpes, 2018
- [59] L. Prejbeanu, "InMRAM School - MRAM Process & Tests", 2018
- [60] K. L. Metlov and Y. P. Lee, *App. Phys. Lett.* **92**, 112506 (2008)

- [61] E. Stoner and E. P. Wohlfarth, *IEEE Tran. Magn.* **27**, 3475 (1991)
- [62] A. Hubert *et al.*, *Magnetic Domains: The Analysis of Magnetic Microstructures*, Berlin: Springer, 1998
- [63] A. Thiaville, *J. Magn. Magn. Mater.* **182**, 5 (1998)
- [64] A. Thiaville, *Phys. Rev. B* **61**, 12221 (2000)
- [65] W. F. Brown Jr., *Phys. Rev* **105**, 1479 (1957)
- [66] M. Chshiev, A. Manchon, A. Kalitsov *et al.*, *Phys. Rev. B* **92**, 104422 (2015)
- [67] J. Grollier, A. Chanthbouala, R. Matsumoto *et al.*, *Comptes Rendus Physique* **12**, 309 (2011)
- [68] M. D. Stiles *et al.*, "Spin-Transfer-Torque and Dynamics", Berlin:Springer, 225 (2006)
- [69] N. Strelkov A. A. Timopheev, R. C. Sousa *et al.*, *Phys. Rev. B* **95**, 184409 (2017)
- [70] J. Z. Sun, S. L. Brown *et al.*, *Phys. Rev. B* **88**, 104426 (2013)
- [71] J. Slonczewski and J. Z. Sun, *J. Magn. Magn. Mater.* **310**, 169 (2007)
- [72] J. Z. Sun and D. C. Ralph, *J. Magn. Magn. Mater.* **320**, 1227 (2008)
- [73] R. Koch, J. A. Katine and J. Z. Sun, *Phys. Rev. Lett.* **92**, 088302 (2004)
- [74] J. Z. Sun, *Phys. Rev. B* **62**, 570 (2000)
- [75] H. Sato, M. Yamanouchi, S. Ikeda *et al.*, *Appl. Phys. Lett.* **99**, 042501 (2011)
- [76] K. Garello, C. O. Avci, I. M. Miron *et al.*, *Appl. Phys. Lett.* **105**, 212402 (2014)
- [77] H. Liu, D. Bedau, J. Z. Sun *et al.* *J. Magn. Magn. Mater* **358**, 223 (2014)
- [78] D. C. Worledge, G. Hu, D. W. Abraham *et al.*, *Appl. Phys. Lett.* **98**, 022501 (2011)
- [79] J. Z. Sun, R. P. Robertazzi, J. Nowak *et al.*, *Phys. Rev. B* **84**, 064413 (2011)
- [80] S. Jamet *et al.*, *Magnetic Nano- and Microwires*, Elsevier 2015
- [81] R. Hertel and J. Kirschner, *Phys. B: Cond. Matt.* **343**, 206 (2004)
- [82] A. Thiaville, Y. Nakatani, J. Miltat *et al.*, *EPL* **69**, 990 (2005)
- [83] H. Kohno *et al.*, *Nanomagnetism and Spintronics*, Elsevier 2009
- [84] B. Chen, J. Lourebam, S. Goolaup *et al.*, *Phys. Lett. A* **382**, 3429 (2018)